Check for updates

Global Biogeochemical Cycles

RESEARCH ARTICLE
10.1029/2025GB009008

Special Collection:
The U.S. GEOTRACES South Pacific and Southern Ocean Transect (GP17-OCE)

High-Latitude Controls on the Silicon Isotope Composition of Silicic Acid in the South Pacific

Julien T. Middleton[1], Mark Holzer[2], Ivia Closset[1,3], Janice Jones[1], and Mark A. Brzezinski[1,4]

[1]Marine Science Institute, University of California, Santa Barbara, CA, USA, [2]Department of Applied Mathematics, School of Mathematics and Statistics, University of New South Wales, Sydney, NSW, Australia, [3]Finnish Meteorological Institute, Helsinki, Finland, [4]Department of Ecology Evolution and Marine Biology, University of California, Santa Barbara, CA, USA

Key Points:

- High-latitude nutrient trapping leads to accumulation of light δ^{30}Si in the Southern Ocean (SO) and the export of heavy δ^{30}Si in mode waters
- Deep-water entrainment accounts for a significant proportion of heavy δ^{30}Si within mode waters across the entire transect
- Observed deep-water δ^{30}Si has a greater range than captured by models, reflecting variation between SO and more northern sources

Supporting Information:

Supporting Information may be found in the online version of this article.

Correspondence to:

J. T. Middleton,
jtmiddleton@ucsb.edu

Citation:

Middleton, J. T., Holzer, M., Closset, I., Jones, J., & Brzezinski, M. A. (2026). High-latitude controls on the silicon isotope composition of silicic acid in the South Pacific. *Global Biogeochemical Cycles*, *40*, e2025GB009008. https://doi.org/10.1029/2025GB009008

Received 4 DEC 2025
Accepted 12 MAY 2026
Corrected 2 JUL 2026

This article was corrected on 2 JUL 2026. See the end of the full text for details.

Author Contributions:

Conceptualization: Mark Holzer, Ivia Closset, Mark A. Brzezinski
Data curation: Janice Jones, Mark A. Brzezinski
Formal analysis: Julien T. Middleton, Mark Holzer, Janice Jones, Mark A. Brzezinski
Funding acquisition: Mark A. Brzezinski
Investigation: Julien T. Middleton, Mark Holzer, Mark A. Brzezinski

© 2026. American Geophysical Union. All Rights Reserved.

Abstract We present measurements of silicon isotopes in silicic acid, δ^{30}Si, from GEOTRACES $GP17_{OCE}$ between 20°S and 60°S along 152°W. The section sampled key water masses, allowing assessment of controls on large-scale δ^{30}Si features. Observational data paralleled results of a data-constrained Si isotope model and are consistent with nutrient trapping and partial nutrient consumption in polar surface waters leading to the accumulation of light silicon isotopes in the deep Southern Ocean (SO) and transport of the residually heavy fraction northward within Sub-Antarctic Mode Water (SAMW) and Antarctic Intermediate Water (AAIW). Deep-water δ^{30}Si values were nearly constant along isopycnals in the South Pacific, with vertical gradients driven by an increasing fractional contribution of isotopically light regenerated silicic acid with depth. Isotope values in deep waters from the SO to Tahiti exhibited a greater range than previously observed in the South Pacific or predicted by models, with δ^{30}Si falling between 1.19‰ and 1.45‰. SAMW and AAIW exhibited relatively heavy, uniform δ^{30}Si. Model results suggest that these mode waters are composed of preformed silicic acid subducted in the outcropping region and regenerated silicic acid sourced in roughly equal measure from polar waters and northern distal sources. Distal input is mainly through entrainment of underlying Upper Circumpolar Deep Water into AAIW.

1. Introduction

The transport of nutrients from the high southern latitudes to the equator by mode and intermediate waters leads to a strong influence of the Southern Ocean (SO) on global biogeochemical cycles, including that of silicic acid (de Souza et al., 2014; Palter et al., 2010; Sarmiento et al., 2004). Diatoms, the predominant biological user of silicic acid, account for 40% of the carbon exported from surface ocean into the deep sea by photosynthetic organisms (Tréguer et al., 2018), making an understanding of silicic-acid cycling imperative for understanding future climate scenarios. Silicon isotopes within silicic acid (δ^{30}Si) offer a window into the controls on this cycling (Sutton et al., 2018). Both observations and models of the global marine silicon cycle suggest that the SO has a strong influence on the global distribution of both silicic acid and δ^{30}Si (Brzezinski et al., 2025; de Souza, Reynolds, Johnson, et al., 2012; de Souza, Reynolds, Rickli, et al., 2012; de Souza et al., 2014; Fripiat et al., 2011; Holzer & Brzezinski, 2015).

High southern latitude processes significantly impact the global structure of silicic acid ($Si(OH)_4$) and δ^{30}Si in deep waters through the partitioning of chemically identical preformed and regenerated silicic acid between the upper and lower limbs of the Meridional Overturning Current (MOC; Brzezinski et al., 2025; de Souza, Reynolds, Rickli, et al., 2012; de Souza et al., 2014; Holzer & Brzezinski, 2015). The preformed pool represents 100% of the silicic-acid concentration found in the euphotic zone and enters the ocean interior through advective-diffusive transport alone. Regenerated silicic acid is by definition zero in the euphotic zone and within the ocean interior is defined as the difference between the total and preformed concentrations that result from the dissolution of biogenic opal exported from the euphotic zone. Because biological opal formation preferentially incorporates the lighter isotopes of Si (De La Rocha et al., 2000; Sutton et al., 2013; Varela et al., 2004), preformed silicic acid is generally isotopically heavier than regenerated silicic acid. This difference is central to how the ocean circulation shapes the global δ^{30}Si distribution.

In the high southern latitudes, isotopically heavy preformed silicic acid is substantial due to the partial consumption of silicic-acid in SO surface waters (Cardinal et al., 2005, 2007; Closset et al., 2015; Fripiat et al., 2012;

19449224, 2026, 5, Downloaded from https://agupubs.onlinelibrary.wiley.com/doi/10.1029/2025GB009008 by Finnish Meteorological, Wiley Online Library on [29/09/2026]. See the Terms and Conditions (https://onlinelibrary.wiley.com/terms-and-conditions) on Wiley Online Library for rules of use; OA articles are governed by the applicable Creative Commons License

Methodology: Julien T. Middleton, Mark Holzer, Janice Jones, Mark A. Brzezinski
Project administration: Mark A. Brzezinski
Software: Julien T. Middleton, Mark Holzer
Supervision: Mark A. Brzezinski
Visualization: Julien T. Middleton, Mark Holzer, Mark A. Brzezinski
Writing – original draft: Julien T. Middleton
Writing – review & editing: Julien T. Middleton, Mark Holzer, Ivia Closset, Mark A. Brzezinski

Varela et al., 2004). Surface waters become further enriched in the heavy isotope as isotopically light silicic acid is preferentially and progressively depleted during northward transport by Ekman drift (Sarmiento et al., 2004; Varela et al., 2004). Heavy preformed δ^{30}Si is ultimately subducted within mode and intermediate waters and transported to the low latitudes (Figure 1b; Beucher et al., 2008; de Souza, Reynolds, Johnson, et al., 2012; de Souza et al., 2014; Holzer & Brzezinski, 2015).

The partitioning of light and heavy silicon isotopes between mode and deep waters is a consequence of nutrient trapping in high southern latitudes (de Souza, Reynolds, Rickli, et al., 2012; de Souza et al., 2014; Holzer & Brzezinski, 2015; Wischmeyer et al., 2003). Dissolution of exported opal transports isotopically light regenerated silicic acid into SO deep waters (Cardinal et al., 2005; Cavagna et al., 2011; Fripiat et al., 2011; Holzer & Brzezinski, 2015; Sarmiento & Gruber, 2006; Varela et al., 2004). Silicic-acid trapping amplifies the accumulation of isotopically light δ^{30}Si as locally produced biogenic opal sinks out of the euphotic zone and dissolves into circulation which returns this regenerated silicic acid back to its surface origin region (Figure 1b; Holzer et al., 2014; Lumpkin & Speer, 2007; Talley, 2013). This cycling exposes silicic acid to multiple cycles of biological productivity and leads to the accumulation of regenerated silicic acid with a particularly light isotopic signature in the deep SO (de Souza, Reynolds, Rickli, et al., 2012; de Souza et al., 2014; Fripiat et al., 2011; Holzer & Brzezinski, 2015).

Thus, isotopically heavy, silicic-acid-poor mode and intermediate waters contrast with deep waters containing high concentrations of isotopically light silicic acid. Mode and intermediate waters flow northward, setting the δ^{30}Si composition of the main thermocline of the Southern Hemisphere and North Atlantic (Beucher et al., 2008; de Souza, Reynolds, Johnson, et al., 2012; Fripiat et al., 2011; Holzer & Brzezinski, 2015), while deep waters flow northward and penetrate beyond the equator in the Pacific and Atlantic Oceans (Lumpkin & Speer, 2007; Talley, 2013), influencing δ^{30}Si across these basins (Brzezinski et al., 2025; de Souza, Reynolds, Rickli, et al., 2012). Mode and intermediate waters undergo subsequent biogeochemical modification during their northward transit into the South Pacific (Holzer & Brzezinski, 2015; Holzer et al., 2014), although the controls on this modification are unexplored for the Si system due to a lack of high-resolution observations in the region.

While models and current data sets have provided a detailed view of global oceanic Si cycling, existing empirical data from the SO are still limited in geographic extent, making it challenging to quantify the large-scale processes at work. Here, we focus on the meridional part of the GEOTRACES GP17$_{OCE}$ campaign (Figure 1a) and do not include the portion of GP17$_{OCE}$ that transited the SO between 150°W and Chile. The meridional transect represents a synoptic full-depth section of observed δ^{30}Si ($\delta^{30}Si_{obs}$) extending from the tropics near Tahiti (20°S) to 60°S in the high southern latitudes, capturing both mode/intermediate and deep waters. By combining our observational analysis with modeling results, we provide a detailed evaluation of the major mechanisms controlling the $\delta^{30}Si_{obs}$ distribution in the South Pacific from high latitudes to the tropics. Our data are consistent with nutrient trapping leading to the accumulation of light silicon isotopes in the SO, while the residually heavy fraction is subducted in mode and intermediate waters. Our findings suggest that mode and intermediate waters also receive a significant proportion of their heavy isotopic signature through entrainment of underlying deep waters, which occurs across the entirety of the transect. The combined influence of the heavy preformed signature subducted from the outcropping regions and entrainment of light deep waters creates nearly constant δ^{30}Si along isopycnals within mode and intermediate waters across the South Pacific.

2. Materials and Methods

2.1. Water Mass and Hydrographic Front Identification

Given the importance of the MOC in the global silicon cycle, we outline the major water masses and associated dynamical hydrographic fronts encountered along GP17$_{OCE}$. A schematic of the MOC modified from Talley (2013) is presented in Figure 1b. Here we consider six globally important water masses: Sub-Antarctic Mode Water (SAMW), Antarctic Intermediate Water (AAIW), Upper and Lower Circumpolar Deep Water (UCDW and LCDW), Pacific Deep Water (PDW), and Antarctic Bottom Water (AABW). SAMW is characterized by a minimum in potential vorticity and isopycnals between $26.80 < \sigma_\theta < 27.06$ kg m^{-3} (Hartin et al., 2011; Talley et al., 2011). SAMW can be tracked into the ocean interior by negative Si* = [Si(OH)$_4$]–[NO_3^-] which quantifies the excess or deficit of Si relative to nitrate (NO_3^-). In the polar SO, iron limitation leads to the strong preferential consumption of silicic acid relative to NO_3^- by diatoms, creating strongly negative Si* which is transported to the subantarctic zone (SAZ) by northward Ekman flow and subsequently subducted with

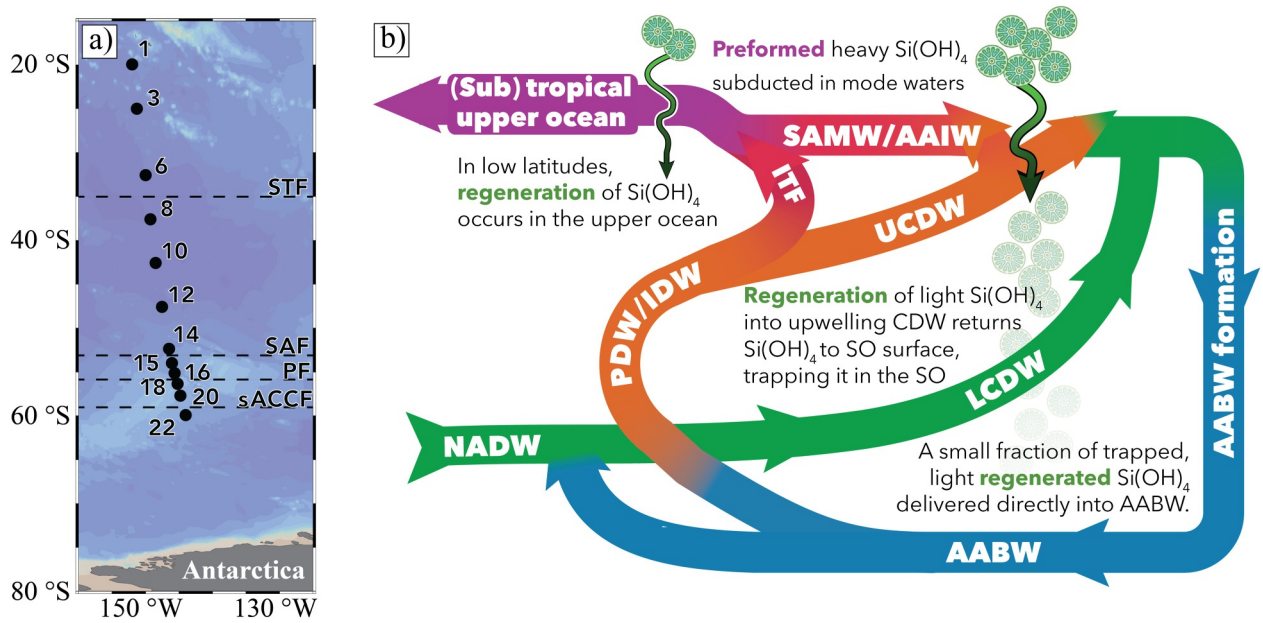


Figure 1. (a) Map showing the stations of the $GP17_{OCE}$ meridional transect in the South Pacific and adjacent Southern Ocean (SO). The latitudes where the major hydrographic fronts cross the transect are defined by the criteria in Section 2.1 and indicated with dashed lines. (b) Schematic of the large-scale meridional overturning circulation of the South Pacific, modified from Talley (2013). Relevant Si-cycling processes are overlaid to highlight the importance of the interplay between physical circulation and biogenic opal rain in setting the large-scale silicic-acid and $\delta^{30}Si$ distributions. Of particular importance is SO nutrient trapping, which imparts $Si(OH)_4$-poor mode and intermediate waters with residually heavy $\delta^{30}Si$ remaining following biological export, and $Si(OH)_4$-rich deep waters with light $\delta^{30}Si$ from dissolving opal rain.

SAMW (Brzezinski et al., 2003; Franck et al., 2000; Sarmiento et al., 2004; Figure 2b). The denser AAIW falls between $27.06 < \sigma_\theta < 27.40$ kg m^{-3}, with the top of the AAIW traced by a minimum in salinity (Hartin et al., 2011; Talley et al., 2011). Along the meridional transect, stations S15 and S16 fell in the SAMW outcropping region, while S18 and S20 fell within the outcropping of AAIW (Figure 1a). Following subduction, SAMW and AAIW undergo subsequent biogeochemical modification during northward transit into the South Pacific oligotrophic gyre (Holzer & Brzezinski, 2015; Holzer et al., 2014).

CDW is composed of NADW, Indian Deep Water (IDW), and PDW, which mix throughout transit in the deep Antarctic Circumpolar Current (ACC). The upper layer of CDW (UCDW) is differentiated from AAIW at the 27.5 kg m^{-3} σ_θ isopycnal and can also be traced as an oxygen minimum layer with dissolved $O_2 < 180$ μmol kg^{-1} (Talley et al., 2011). Of the deep-water sources to CDW, UCDW receives most of its inputs from IDW and PDW (~70%; Talley, 2013). Within the Pacific, some IDW and PDW are returned to the upper limb of the MOC through the Indonesian Flow Through (ITF). As the ITF resides in the western margin of the Pacific far from the $GP17_{OCE}$ meridional transect, it will not be discussed further here. On the same isopycnal as UCDW is PDW, which forms within the deep Pacific through a mixture of modified UCDW and upwelled deep waters with no surface sources (Talley et al., 2011). Because PDW forms internally from waters flowing in from the SO, it can be identified by a very high radiocarbon age, no CFCs, and low dissolved O_2, as well as high macronutrients (Talley et al., 2011). Along $GP17_{OCE}$, PDW is best distinguished from UCDW by elevated macronutrients ($[NO_3^-] > 35$ μmol L^{-1}) and a mid-depth oxygen minimum ($[O_2] \leq 155$ μmol L^{-1}), which indicate PDW inflow between 2,000–3,000 m from S1 (20°S) to S8 (37.5°S) (Figures S1a and S1b in Supporting Information S1; Talley et al., 2011). The lower half of CDW (LCDW) is a high-$[Si(OH)_4]$, high-salinity water mass that upwells adiabatically in the SO, but never reaches the surface (Talley, 2013). Instead, LCDW mixes with dense Antarctic waters and undergoes cooling and freshening, leading to downwelling, which returns a portion of LCDW to the deep ocean as AABW. Of the deep-water sources to LCDW, nearly half of its volume comes from dense NADW, with the remainder comprised of IDW and PDW (Talley, 2013). We use the AABW definition of Talley et al. (2011), which distinguishes pure AABW from LCDW at the 28.27 kg m^{-3} γ_n neutral density isopycnal. Pure AABW is confined to the SO by bathymetric ridges surrounding the Antarctic Plate, such as the Pacific-Antarctic

19449224, 2026, 5, Downloaded from https://agupubs.onlinelibrary.wiley.com/doi/10.1029/2025GB009008 by Finnish Meteorological, Wiley Online Library on [29/09/2026]. See the Terms and Conditions (https://onlinelibrary.wiley.com/terms-and-conditions) on Wiley Online Library for rules of use; OA articles are governed by the applicable Creative Commons License

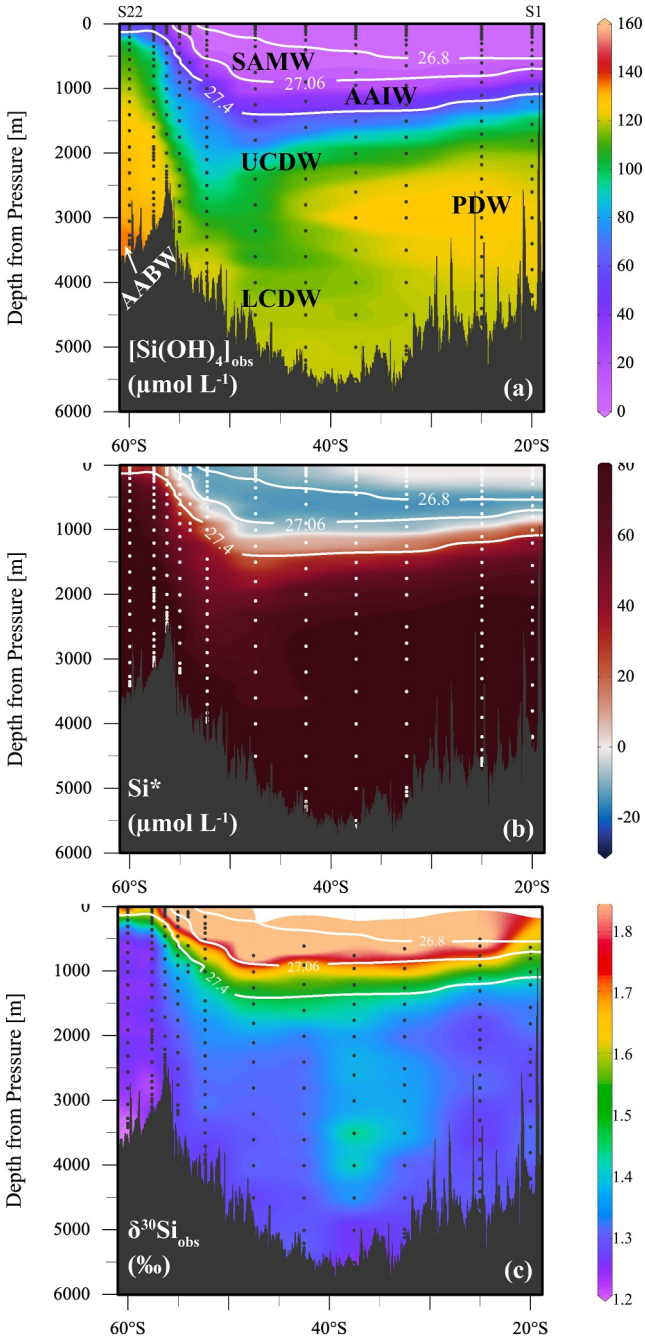


Figure 2. Observed spatial distribution of (a) silicic-acid concentration $[Si(OH)_4]_{obs}$ (μmol kg^{-1}), (b) Si* = $[Si(OH)_4]_{obs}$–$[NO_3^-]$, and (c) silicon isotopes in silicic acid as $\delta^{30}Si_{obs}$ along the $GP17_{OCE}$ meridional transect. The potential densities bracketing mode and intermediate waters are shown as white contours, and water masses are labeled in (a) based on the criteria of Section 2.1. Dots indicate the locations of the water samples analyzed.

Ridge encountered at S18 (56.3°S) and S20 (57.6°S). Thus, we sampled pure AABW at S22 along $GP17_{OCE}$. The average $[Si(OH)_4]_{obs}$, $\delta^{30}Si_{obs}$, and water-mass identification criteria can be found in Table 1.

The circulation of these water masses produces dynamic hydrographic fronts that influence local biogeochemistry. $GP17_{OCE}$ traverses the Sub-Tropical Front (STF), Subantarctic Front (SAF), Polar Front (PF), and the southern Antarctic Circumpolar Front (sACCF) (Figure 1a). The STF was crossed near 35°S between S6 and S8, as delineated by significant meridional gradients in temperature (≥4°C) and salinity (≥0.5) in the upper ocean accompanied by steep thermoclines and haloclines. The occurrence of the sharp 4–5°C isotherm at ~200 m depth just south of S14 indicated that the SAF was crossed near ~53°S (Orsi et al., 1995) very near the SAF position determined using regional float data from previous years (Williams et al., 2016). The PF was crossed between S16 (55.0°S) and S18 (56.3°S), as identified by the northernmost extent of the 2°C isotherm surrounding the temperature minimum in the upper 200 m of the surface ocean (Talley et al., 2011). Stations 18 and 20 both sat within the outcropping AAIW and within the region between the PF and southern ACC Front (sACCF), referred to as the Polar Frontal Zone (PFZ; Figure 1a). The PFZ marks the effective northern boundary of UCDW upwelling to the surface of the SO (Talley et al., 2011). The sACCF was identified by the potential temperature minimum in the surface of $\theta < 0$°C (Talley et al., 2011) and was crossed between S20 (57.6°S) and S22 (60.0°S).

2.2. Sample Collection

Seawater samples for the measurement of $\delta^{30}Si$ in $Si(OH)_4$ were collected during GEOTRACES $GP17_{OCE}$ aboard the R/V Roger Revelle (RR2214) from November 2022 to January 2023 (Figure 1a). The cruise track proceeded from near Tahiti at 20°S southward generally along the 152°W longitude to 67°S, before proceeding east along the 67°S meridian until arrival at the Chilean shelf near 75°W. Here, we analyze the meridional portion of the transect between S1 (20°S) and S22 (60°S), comprising full depth profiles at 11 stations and one station (S15) with a depth profile of 1,000 m. All samples were collected using the conventional 36-place Ocean Data Facility rosette, which was equipped with 10 L Niskin bottles and the standard CTD package. Up to four liters of seawater were filtered directly from each depth into high-density polyethylene bottles using Teflon-lined Tygon tubing in line with an AcroPak® 500 capsule filter containing dual (0.8 μm/0.45 μm Supor® membrane filters). Capsule filters and sample bottles were acid cleaned prior to the cruise and well rinsed with sample water immediately prior to sample collection following Cutter et al. (2017). AcroPak® capsule filters were kept refrigerated between sample collections and replaced at every few stations. Filled sample bottles were capped and stored in pallet boxes on deck at ambient temperature without any preservative. Samples were monitored throughout the duration of the cruise and did not freeze at any point.

2.3. Sample Preparation and Measurement of $[Si(OH)_4]_{obs}$ and $\delta^{30}Si_{obs}$

Seawater $Si(OH)_4$, nitrate, and phosphate concentrations were measured at sea after allowing samples to warm to room temperature on a Seal Analytical continuous-flow Auto Analyzer 3 following Becker et al. (2019). Dissolved oxygen concentrations were measured at sea using an automated oxygen titrator following (Langdon, 2010). These data are reported by Twining et al. (2025).

19449224, 2026, 5, Downloaded from https://agupubs.onlinelibrary.wiley.com/doi/10.1029/2025GB009008 by Finnish Meteorological, Wiley Online Library on [29/09/2026]. See the Terms and Conditions (https://onlinelibrary.wiley.com/terms-and-conditions) on Wiley Online Library for rules of use; OA articles are governed by the applicable Creative Commons License

19449224, 2026, 5, Downloaded from https://agupubs.onlinelibrary.wiley.com/doi/10.1029/2025GB009008 by Finnish Meteorological, Wiley Online Library on [29/09/2026]. See the Terms and Conditions (https://onlinelibrary.wiley.com/terms-and-conditions) on Wiley Online Library for rules of use; OA articles are governed by the applicable Creative Commons License

Table 1
Average $[Si(OH)_4]_{obs}$ and $\delta^{30}Si_{obs}$ Composition of Water Masses Present Along $GP17_{OCE}$

Watermass	Mean $[Si(OH)_4]_{obs}$ ($\mu mol\ kg^{-1}$)	±1SE	Mean $\delta^{30}Si_{obs}$ (‰)	±1SE	n	Criteria
SAMW	10	4	+1.90	0.2	18	$26.8 \leq \sigma_\theta \leq 27.06$
AAIW	32	14	+1.70	0.2	23	$27.06 \leq \sigma_\theta \leq 27.4$
UCDW	96	23	+1.35	0.05	40	$\sigma_\theta > 27.5\ kg\ m^{-3}$ with $[O_2] < 180\ \mu mol\ kg^{-1}$
PDW	116	8	+1.33	0.02	15	Stations 1–10 with $[NO_3^-] \geq 35\ \mu mol\ kg^{-1}$, $27.5 > \sigma_\theta$, and $[O_2] \leq 155\ \mu mol\ kg^{-1}$
LCDW	114	11	+1.28	0.05	85	$z > 500$ m and CTDSAL > 34.7
AABW	133	2	+1.22	0.03	7	$\gamma_n \geq 28.27\ kg\ m^{-3}$

Note. Criteria used to define water masses come from Talley et al. (2011).

Samples were prepared for Si isotope analysis following the protocol described by Brzezinski et al. (2025). Seawater aliquots containing 5–30 μmols of $Si(OH)_4$ were processed for silicon isotope measurements. Samples with $[Si(OH)_4] < 5\ \mu mol\ L^{-1}$ were not processed due to analytical limitations. Along the $GP17_{OCE}$ meridional transect, samples with <5 μmol L^{-1} occurred in the South Pacific gyre surface (<500 m, S1–14) and the mixed layer of the SAMW outcropping region (<100 m, S14–16). In all other samples, seawater aliquots containing 5–30 μmols of $Si(OH)_4$ were reacted with triethylamine-ammonium molybdate (TEA-moly) with a volumetric ratio of 0.6 TEA-moly:1 seawater to precipitate triethylamine-silicomolybdic acid. The precipitate was combusted to form solid SiO_2 as cristobalite (Brzezinski et al., 2006; C. L. De La Rocha et al., 1996) dissolved it in 7.5 M hydrofluoric acid (HF) and precipitated it as Cs_2SiF_6 by the addition of CsCl. The mixture was separated by centrifugation, the supernatant removed, and the solid rinsed with ethanol before being dried at 65°C. Following this, separation by centrifugation, supernatant removal, and rinsing of the solid was carried out again with ethanol and a final time with methanol, with appropriate drying at 65°C after each rinse. Conversion to $BaSiF_6$ was then carried out by the addition of $BaCl_2$. $BaSiF_6$ went through a similar centrifugation process with only the rinse fluid changing: this solid was rinsed twice with methanol and once with ethanol.

Isotopic analysis was carried out on a Nu Sil inlet system coupled to a Nu Perspective isotope-ratio mass spectrometer at the University of California–Santa Barbara through the thermal decomposition of the $BaSiF_6$ solid to solid BaF_2 and SiF_4 gas. Silicon isotopes were measured at *m/z* 85, 86, and 87, corresponding to the ion, SiF_3^+. The primary $\delta^{30}Si$ standard NIST NBS28 (RM8546) and two well-characterized secondary standards, Big Batch and Diatomite (Grasse et al., 2017; Reynolds et al., 2007), were analyzed at the beginning and end of every run (50 samples). The Diatomite standard was measured twice at regular intervals in all run sessions to monitor instrumental drift. Drift was not observed in any measurement session. The reference seawater $ALOHA_{1000}$ (Grasse et al., 2017) was included periodically to assess measurement accuracy. Seawater samples (as $BaSiF_6$) were analyzed in duplicate to quadruplicate, with all replicate measurements made in separate analytical sessions. Select samples were reprocessed multiple times from seawater to $BaSiF_6$ to evaluate the isotopic variation related to chemical preparation.

Silicon isotope values of seawater samples were calculated using the multi-point calibration method of Paul et al. (2007): the measured $\delta^{30}Si$ for all three reference materials were regressed against their consensus $\delta^{30}Si$ values. Standardized sample values were then calculated using the regression line of the standards. The regression approach produces a smaller normalization error than the single-point normalization to NBS28 as it is more robust against random analysis error on any one standard (Paul et al., 2007).

2.4. Data Quality Control

Analytical precision, as assessed by the repeated analysis of a single chemical preparation of sample GT# 17490 (57.6°S, 145°W, z = 202 m), resulted in an average standard error in $\delta^{30}Si$ of 0.02‰ (n = 5; Table S1 in Supporting Information S1). Variation in measured $\delta^{30}Si$ associated with chemical preparation was quantified by preparing and analyzing a single sample, GT# 18107 (67°S, 115°W, z = 4,249 m), five independent times. The standard error across the five preparations was 0.03‰ (Table S1 in Supporting Information S1). However, as most samples were measured fewer than five times and chemically prepared for analysis once, we also report the average standard error across all samples to offer a more representative estimate of measurement precision across

19449224, 2026, 5, Downloaded from https://agupubs.onlinelibrary.wiley.com/doi/10.1029/2025GB009008 by Finnish Meteorological, Wiley Online Library on [29/09/2026]. See the Terms and Conditions (https://onlinelibrary.wiley.com/terms-and-conditions) on Wiley Online Library for rules of use; OA articles are governed by the applicable Creative Commons License

Table 2
δ^{30}Si Values of Primary and Secondary Si Isotope Standards and Reference Seawater

Standard material	Measured δ^{30}Si (‰)	1SD	n	Consensus δ^{30}Si (‰)	1SD	Reference
NBS28	0.03	0.03	97	0	0	
Big Batch	−10.44	0.08	191	−10.48	0.27	Reynolds et al. (2007)
Diatomite	1.24	0.04	195	1.26	0.1	Reynolds et al. (2007)
ALOHA1000m	1.29	0.03	10	1.24	0.1	Grasse et al. (2017)

the data set. This was found to be 0.03‰ ($\overline{1SE}$, $n = 419$). Analytical accuracy was determined by the comparison of consensus and measured values for the primary Si isotope reference material NBS28 (quartz), the secondary reference materials Big Batch (cristobalite) and Diatomite (calcined diatomite), and the reference seawater $ALOHA_{1000}$ (Grasse et al., 2017; Reynolds et al., 2007). Consensus and measured δ^{30}Si agree to within 0.05‰ for all materials (Table 2).

Station 1 of $GP17_{OCE}$ reoccupied the same geographic location, 152°W and 20°S, as a previous GEOTRACES cruise (GP15, S39). The $\delta^{30}Si_{obs}$ data for this location from both cruises are shown in Figure S2 in Supporting Information S1. This crossover station allows a further assessment of data quality, with the expectation that $\delta^{30}Si_{obs}$ will be similar over time at the same location. Data from depths >300 m are used for this comparison, as varying degrees of $Si(OH)_4$ consumption by organisms leads to associated variation in $\delta^{30}Si_{obs}$ in the euphotic zone. Silicic acid is used to align data from the cruises, as $\delta^{30}Si_{obs}$ is strongly related to concentration, thereby allowing comparison of samples that were measured at slightly offset depths between cruises. Both data sets were generated using the isotope preparation protocol described in Section 2.3. The data sets generally agree within 0.1‰ or better, with the strongest coherence seen in deep waters below ∼1,600 m (Brzezinski, 2024; Brzezinski et al., 2026).

2.5. Model Methods

To gain insight into processes that shape the large-scale meridional structure of δ^{30}Si in the South Pacific and adjacent SO, we use the simple data-constrained steady-state Si- and δ^{30}Si-cycling model of Holzer et al. (2014) and Holzer and Brzezinski (2015), as recently updated by Brzezinski et al. (2025). Biological uptake of $Si(OH)_4$ is modeled by conditional restoration within the euphotic zone to $[Si(OH)_4]_{obs}$ from the World Ocean Atlas 2018 (WOA18; Garcia et al., 2018). A steady-state Si cycle is maintained by the addition of a small, spatially uniform surface source that may be regarded as a simplified representation of riverine input homogenized over the surface ocean. The magnitude of the surface source is the observed global mean $[Si(OH)_4]$ of 86.2 μmol kg^{-1} per 50 years. We prescribed a biological uptake timescale of 10.5 days and optimized the opal sinking speed (38.7 m d^{-1}) and burial fraction (10.6%) by minimizing the volume-weighted globally integrated quadratic mismatch between modeled $[Si(OH)_4]$ and the WOA18 observations. Biogenic opal is modeled to sink at a constant, globally uniform terminal speed and dissolve to $Si(OH)_4$ with a temperature-dependent Arrhenius factor (Gnanadesikan, 1999). A fraction of the opal that sinks to the ocean bottom is permanently removed from the system as a simple representation of sediment burial. Sediment pore waters are not modeled and there are no $Si(OH)_4$ contributions from the seafloor, either by pore-water efflux or hydrothermal activity. The parameters of the Si isotope model were tuned against available observations (Brzezinski & Jones, 2015; de Souza, Reynolds, Johnson, et al., 2012; de Souza, Reynolds, Rickli, et al., 2012; see supplementary Figures S2 and S3 of Brzezinski et al., 2025 for a plot of modeled versus observed values for $Si(OH)_4$ and δ^{30}Si). Fractionation occurs only during opal formation; we did not include any other fractionation mechanisms.

Our Si model is embedded in the 48-level version of the Ocean Circulation Inverse Model with 2° × 2° horizontal resolution (OCIM2-48L; Holzer et al., 2021), which provides a data-assimilated advection-diffusion flux-divergence operator for the ocean circulation. OCIM2-48L is constrained by linearized ocean dynamics (DeVries & Primeau, 2011) and by observations of potential temperature, salinity, CFC-11, CFC-12, natural radiocarbon (Δ^{14}C), and natural δ^3He, with a prescribed diapycnal diffusivity as estimated from tidal mixing (De Lavergne et al., 2020).

We used the model to partition $[Si(OH)_4]$ and δ^{30}Si into their preformed and regenerated components and to partition these further according to the surface location of either last ventilation or biological export, respectively

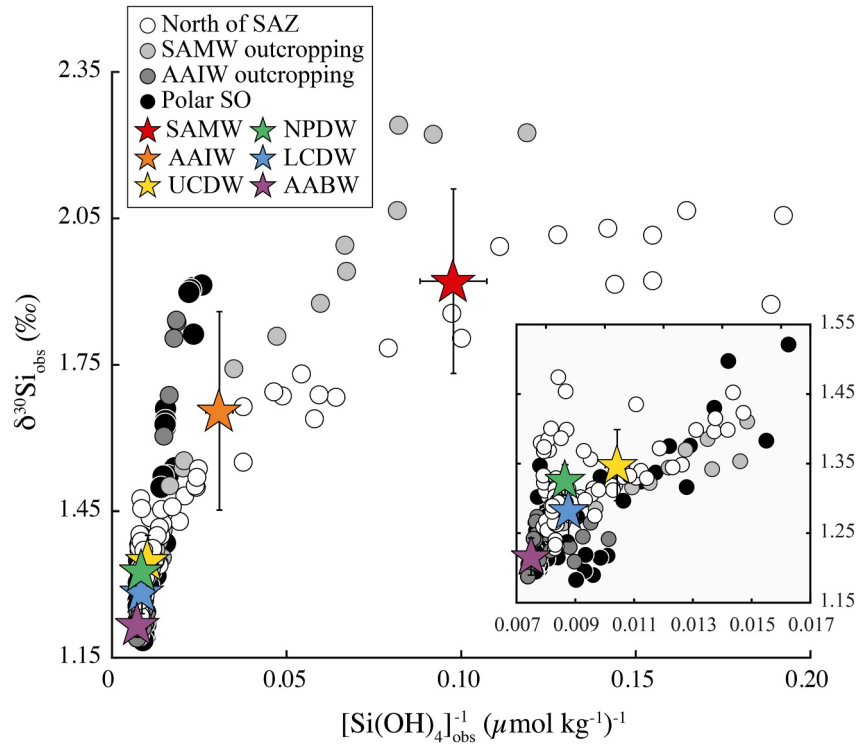


Figure 3. Silicon isotope systematics along the meridional section of GP17oce plotted as mixing diagrams of $\delta^{30}Si_{obs}$ versus $[Si(OH)_4]_{obs}^{-1}$. Circle colors refer to the four surface-origin regions used to partition model results, as described in Section 2.4, while stars represent average water-mass properties based on the criteria in Table 1. All samples are shown. The mixing diagram exhibits multiple quasi-linear relationships between $\delta^{30}Si_{obs}$ and $[Si(OH)_4]_{obs}^{-1}$ in the upper ocean. These intersect near $\delta^{30}Si_{obs}$ ~+1.30‰ and $[Si(OH)]_4]^{-1}$ between 0.008 and 0.0085 (μmol kg^{-1})$^{-1}$, with σ_θ between 27.80 and 27.84 kg m^{-3}. The inset focuses on the Si isotope systematics of the deep Pacific and PFZ where neutral density γ_n > 27.7 kg m^{-3}. Although there is some deviation in the deep waters related to non-linear mixing with the surface of the Southern Ocean (Section 3.1.3), the three average water-mass properties of UCDW, LCDW, and Antarctic Bottom Water obey a linear relationship with $R^2 = 0.999$.

(i.e., "surface origin"). This is done efficiently using an adjoint formulation similar to that used for water itself by Holzer et al. (2021) except both transport by water and sinking biogenic opal are considered for $Si(OH)_4$ in addition to the relevant sources and sinks. The ability to trace the fractional contributions and $\delta^{30}Si$ of preformed and regenerated $Si(OH)_4$ separately without predefined water-mass endmembers (Holzer & Brzezinski, 2015; Holzer et al., 2014) is a significant benefit of our approach. This tracing ability is especially powerful given that no analytical method currently exists to separate preformed and regenerated $Si(OH)_4$. To summarize the contributions to key water masses from the preformed and regenerated $[Si(OH)_4]$ and $\delta^{30}Si$ fields, we partition the global ocean surface into four regions: (a) the global ocean north of the SAZ, the outcropping regions of both (b) SAMW and (c) AAIW, and (d) the polar SO. These nominal regions are defined in the model as the euphotic zone (<100 m) bounded laterally by σ_θ (a) <26.8 kg m^{-3}, (b) 26.8–27.06 kg m^{-3}, (c) 27.06–27.4 kg m^{-3}, and (d) >27.4 kg m^{-3}, as shown in Figures 8 and 9 as demarcated by magenta lines.

We also used our Si model to assess the surface origin of the $Si(OH)_4$ contained in the modeled SAMW and AAIW sub-volumes. The interior sub-volumes of SAMW and AAIW are defined as occurring at depths ≥100 m between longitudes 150°W and 154°W and between the 26.8–27.06 kg m^{-3} and 27.06–27.4 kg m^{-3} σ_θ bounds, respectively. In the case of the AAIW, the southern boundary of the sub-volume is truncated at 55°S to exclude Antarctic Surface Water. However, because only depths below 100 m are included in the sub-volumes, this truncation has negligible consequence.

19449224, 2026, 5, Downloaded from https://agupubs.onlinelibrary.wiley.com/doi/10.1029/2025GB009008 by Finnish Meteorological, Wiley Online Library on [29/09/2026]. See the Terms and Conditions (https://onlinelibrary.wiley.com/terms-and-conditions) on Wiley Online Library for rules of use; OA articles are governed by the applicable Creative Commons License

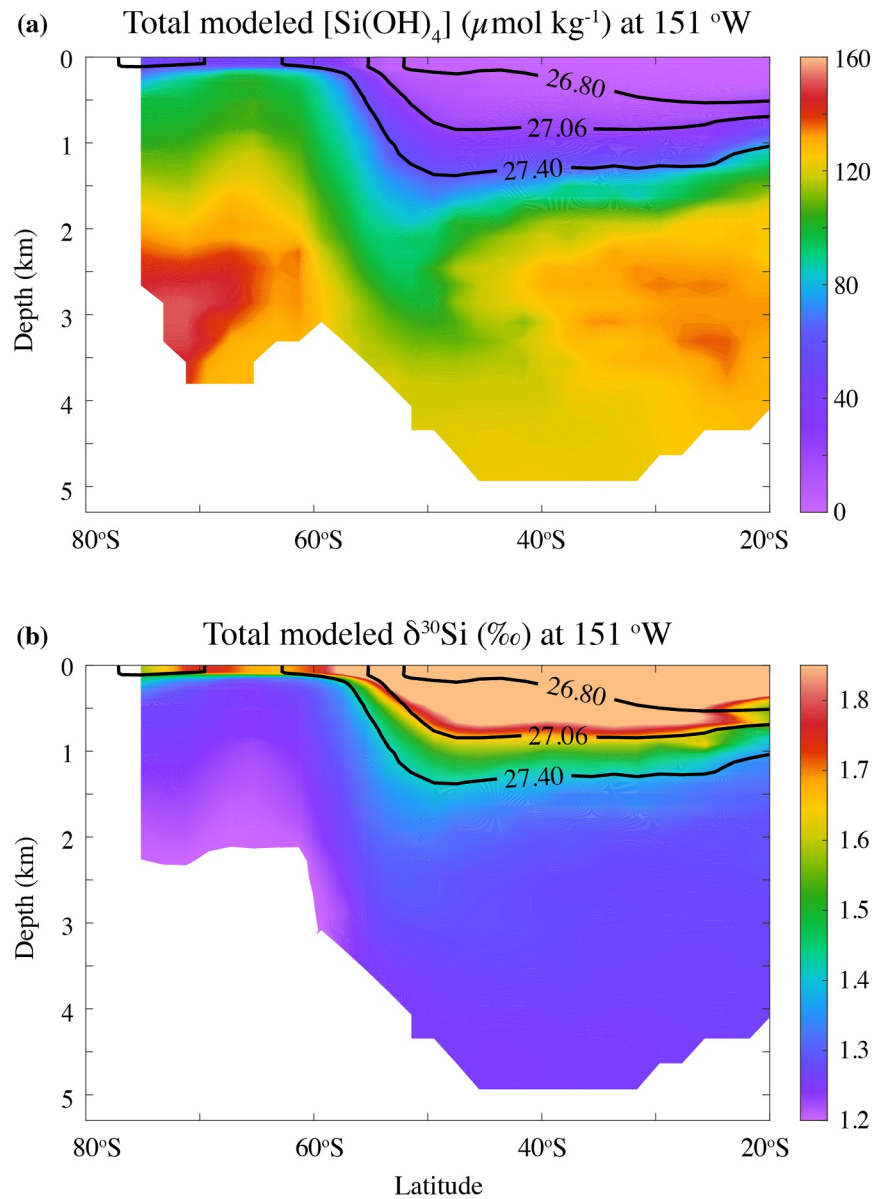


Figure 4. Meridional structure of modeled (a) $[Si(OH)_4]$ and (b) $\delta^{30}Si$ along the $GP17_{OCE}$ meridional transect at 151°W. The Si model does not include inputs from the sea floor such as hydrothermal activity and sediment efflux but is otherwise faithful to the observations (see also Brzezinski et al., 2025 for a more detailed model-observation comparison). The isotopically very light, silicic-acid-rich deep Southern Ocean (SO) is consistent with deep opal dissolution and SO nutrient trapping (Holzer et al., 2014) as well as incomplete $Si(OH)_4$ drawdown by biology due to iron limitation, captured implicitly in the model by conditionally restoring euphotic $[Si(OH)_4]$ to observed concentrations. We include the isopycnals defining the locations of Sub-Antarctic Mode Water and Antarctic Intermediate Water.

3. Results

3.1. Observed Silicic Acid and $\delta^{30}Si$ Along the $GP17_{OCE}$ Meridional Transect

3.1.1. Silicic-Acid Distribution

Silicic-acid concentration showed a large dynamic range from very low in the surface of the oligotrophic gyre, where $[Si(OH)_4]_{obs} < 1$ μmol kg^{-1}, to the highly concentrated in the AABW of the deep SO, where $[Si(OH)_4]_{obs}$ reached 135 μmol kg^{-1} (Figure 2a). Across the $GP17_{OCE}$ transect, observed silicic-acid concentrations generally follow isopycnals. Within SAMW ($26.8 < \sigma_\theta < 27.06$ kg m^{-3}), $[Si(OH)_4]_{obs}$ was relatively constant at

19449224, 2026, 5, Downloaded from https://agupubs.onlinelibrary.wiley.com/doi/10.1029/2025GB009008 by Finnish Meteorological, Wiley Online Library on [29/09/2026]. See the Terms and Conditions (https://onlinelibrary.wiley.com/terms-and-conditions) on Wiley Online Library for rules of use; OA articles are governed by the applicable Creative Commons License

19449224, 2026, 5, Downloaded from https://agupubs.onlinelibrary.wiley.com/doi/10.1029/2025GB009008 by Finnish Meteorological, Wiley Online Library on [29/09/2026]. See the Terms and Conditions (https://onlinelibrary.wiley.com/terms-and-conditions) on Wiley Online Library for rules of use; OA articles are governed by the applicable Creative Commons License

10 ± 4 μmol kg^{-1} ($n = 18$, ±1SE) and increased with depth to an average of 32 ± 14 μmol kg^{-1} ($n = 23$, ±1SE) within AAIW ($27.06 < \sigma_\theta < 27.4$ kg m^{-3}). Silicic-acid concentrations were elevated within the region of PDW inflow, with $[Si(OH)_4]_{obs} = 116 \pm 8$ μmol kg^{-1} ($n = 15$, ±1SE), compared to UCDW found on the same isopycnal outside of this region, which had $[Si(OH)_4]_{obs} = 96 \pm 23$ μmol kg^{-1} ($n = 40$, ±1SE). Below UCDW, LCDW carried 114 ± 11 μmol kg^{-1} ($n = 85$, ±1SE) of dissolved $Si(OH)_4$. Approaching the PF, adiabatic upwelling of UCDW delivered $Si(OH)_4$-rich waters to the surface (Talley, 2013), leading to $Si(OH)_4$-replete high-latitude surface waters with an average concentration of 53.5 ± 0.4 μmol kg^{-1} ($n = 2$, ±1SE). Along the entirety of the meridional transect, AABW had an average silicic-acid concentration of 133 ± 2 μmol kg^{-1} ($n = 7$, ±1SE), in agreement with previous measurements (Cardinal et al., 2005).

3.1.2. $\delta^{30}Si_{obs}$ Distribution Within Silicic Acid Along $GP17_{OCE}$

Silicon isotope values in $Si(OH)_4$ are generally heavy in surface waters and become lighter with depth (Figure 2c). Like the $Si(OH)_4$ distribution, $\delta^{30}Si_{obs}$ contours at depth largely follow isopycnals. Within SAMW, $\delta^{30}Si_{obs}$ had an isotopically heavy signature of $+1.9 \pm 0.2$‰ ($n = 18$, ±1SE). Some samples contained $[Si(OH)_4] < 5$ μmol kg^{-1}, for which isotope data are currently not measurable such that the true isotopic composition of SAMW in the South Pacific is likely heavier than the average given here. The deeper AAIW also showed enrichment with an average $\delta^{30}Si_{obs}$ of $+1.7 \pm 0.2$‰ ($n = 23$, ±1SE), similar to $\delta^{30}Si_{obs}$ in AAIW in the SE Pacific (de Souza, Reynolds, Rickli, et al., 2012). Descending into the underlying UCDW, $\delta^{30}Si_{obs}$ decreased to $+1.35 \pm 0.05$‰ ($n = 40$, ±1SE), while PDW on the same isopycnal in the northern end of the transect was slightly lighter with $\delta^{30}Si_{obs} = +1.33 \pm 0.02$‰ ($n = 15$, ±1SE). Isotopic signatures within UCDW and PDW align with previous studies (Closset et al., 2016; Fripiat et al., 2011; Grasse et al., 2020). Within the deep South Pacific, LCDW was found to have an average $\delta^{30}Si_{obs}$ of $+1.28 \pm 0.05$‰ ($n = 85$, ±1SE), similar to LCDW observed in the eastern tropical Pacific (Grasse et al., 2020). (The elevated $\delta^{30}Si_{obs}$ within deep waters near the STF (37.5°S) are out of the scope of this work but will be addressed in a forthcoming study.) South of the PFZ, elevated $\delta^{30}Si_{obs}$ was observed throughout the surface (Figure 2c), with an average value of $+1.839 \pm 0.003$‰ ($n = 2$, ±1SE). In the deep polar SO, AABW had an average $\delta^{30}Si_{obs}$ of $+1.22 \pm 0.03$‰ ($n = 7$, ±1SE), in agreement with previous measurements (Table 1; Cardinal et al., 2005; de Souza, Reynolds, Johnson, et al., 2012; de Souza, Reynolds, Rickli, et al., 2012; Fripiat et al., 2011).

3.1.3. Mixing Along the Meridional Transect of $GP17_{OCE}$

Plotting $\delta^{30}Si_{obs}$ versus $[Si(OH])_4]^{-1}$ revealed varying Si systematics in the South Pacific and adjacent SO. (On such a plot, a linear relation indicates conservative mixing.) Four hydrographic zones show distinct relationships between $\delta^{30}Si$ and $[Si(OH])_4]^{-1}$: north of the SAZ (S1–S14), in the SAMW outcrop region (S15–S16), in the AAIW outcrop (S18–S20), and south of the PF (S22; Figure 3). Despite diverging in the upper ocean, these data converge near $\delta^{30}Si_{obs} \sim +1.30$‰ and $[Si(OH])_4]^{-1}$ between 0.008 and 0.0085 $(\mu mol\ kg^{-1})^{-1}$, with σ_θ between 27.80 and 27.84 kg m^{-3}. de Souza, Reynolds, Rickli, et al. (2012) observed a similar intersection in the Atlantic basin occurring at significantly heavier $\delta^{30}Si_{obs}$ of +1.55–1.6‰ with $[Si(OH])_4]^{-1}$ between 0.09–0.06 $(\mu mol\ kg^{-1})^{-1}$ and σ_θ between 26.75 and 27.00 kg m^{-3}.

Below the intersection of the upper-ocean data, small differences among deep-water masses are resolved (Figure 3, inset). Previously, modeling of Pacific deep waters suggested isotopic homogeneity in the Si system, with no large variations in $\delta^{30}Si_{obs}$ when $[Si(OH)_4]_{obs} > 120$ μmol kg^{-1} (de Souza et al., 2014; Gao et al., 2016; Wischmeyer et al., 2003). However, recent work by Brzezinski et al. (2025) showed that both observations and model results feature small gradients in the deep waters of the North Pacific when data were averaged across relatively broad geographic regions. Along the $GP17_{OCE}$ meridional transect, we observed a distinct structure in $\delta^{30}Si_{obs}$ following major water mass delineations, including within deep waters where $\gamma_n > 27.7$ kg m^{-3} (Figure 2c). Deep-water $\delta^{30}Si_{obs}$ fell between +1.18 and +1.45‰. Within the subset of samples where $[Si(OH)_4] > 120$ μmol kg^{-1}, the range of $\delta^{30}Si_{obs}$ was 1.19–1.40‰, encompassing a 0.21‰ range that is well outside the average measurement uncertainty ($\overline{1SE} = 0.03$‰).

The large range compared to the analytical precision allowed us to characterize the average $\delta^{30}Si_{obs}$ in UCDW, LCDW, AABW, and PDW (Figure 3, inset). The average $[Si(OH)_4]_{obs}$ and $\delta^{30}Si_{obs}$ for each water mass considered are given in Table 1. Within the deep waters of the $GP17_{OCE}$ meridional transect, the average $\delta^{30}Si_{obs}$/$[Si(OH)_4]_{obs}$ of UCDW, LCDW, and AABW fall along a well-defined mixing line with $R^2 = 0.999$ (Figure 3

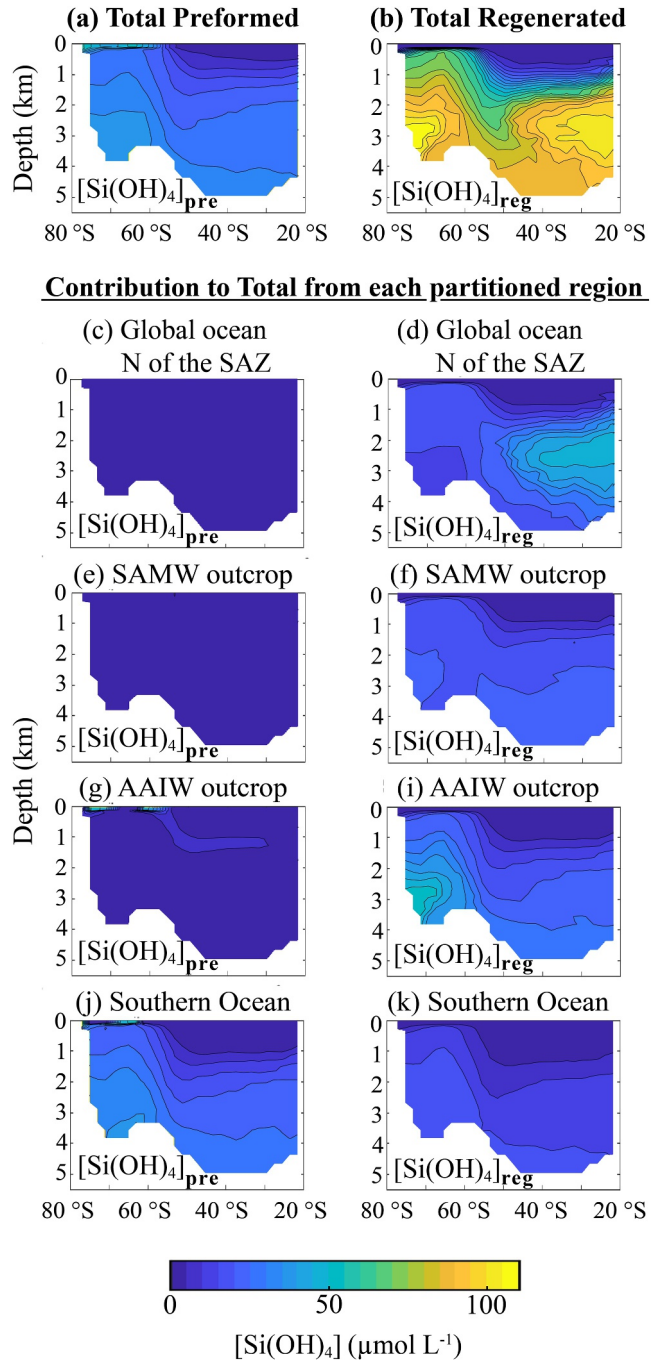


Figure 5. Modeled total (a) preformed $[Si(OH)_4]_{pre}$ and (b) regenerated $[Si(OH)_4]_{reg}$ partitioned according to their euphotic origin in four surface regions (c)–(k). Four surface-origin regions were chosen: the global ocean north of the subantarctic zone (SAZ) as defined by the 26.8 kg m^{-3} isopycnal (c, d), the outcrop of the Sub-Antarctic Mode Water (SAMW) (26.8 kg $m^{-3} < \sigma_\theta < 27.06$ kg m^{-3}; (e, f), the outcrop of the Antarctic Intermediate Water (27.06 kg $m^{-3} < \sigma_\theta < 27.4$ kg m^{-3}; (g, i), and the polar Southern Ocean south of the outcrop of the 27.4 kg m^{-3} isopycnal (j, k). (For maps of these regions, see Figures 8 and 9). We note that $[Si(OH)_4]_{pre}$ contributed to the SAMW from the SAMW outcrop in (e) is near 5 μmol kg^{-1}, although with the color scale shared by all panels this is not visible. The global ocean north of the SAZ (c) makes a negligible contribution to $[Si(OH)_4]_{pre}$.

19449224, 2026, 5, Downloaded from https://agupubs.onlinelibrary.wiley.com/doi/10.1029/2025GB009008 by Finnish Meteorological, Wiley Online Library on [29/09/2026]. See the Terms and Conditions (https://onlinelibrary.wiley.com/terms-and-conditions) on Wiley Online Library for rules of use; OA articles are governed by the applicable Creative Commons License

19449224, 2026, 5, Downloaded from https://agupubs.onlinelibrary.wiley.com/doi/10.1029/2025GB009008 by Finnish Meteorological, Wiley Online Library on [29/09/2026]. See the Terms and Conditions (https://onlinelibrary.wiley.com/terms-and-conditions) on Wiley Online Library for rules of use; OA articles are governed by the applicable Creative Commons License

inset), with UCDW containing the lowest $[Si(OH)_4]_{obs}$ and heaviest $\delta^{30}Si_{obs}$ and AABW containing high $[Si(OH)_4]_{obs}$ that is isotopically light. Lower CDW falls along the mixing line between UCDW and AABW. The northern-sourced PDW has similar $[Si(OH)_4]_{obs}$ and 0.05‰ heavier $\delta^{30}Si_{obs}$ when compared to LCDW, although the isotopic difference is within uncertainty (Figure 3, inset). In the PFZ, deep waters approaching the surface show deviations from the general trend of deep waters, with less $[Si(OH)_4]_{obs}$ than expected based on $\delta^{30}Si_{obs}$ (black dots, Figure 3, inset). This deviation is caused by strong cabbeling with the mixed layer of the PFZ, which creates a water mass denser than either of its parents and mixes the comparatively $[Si(OH)_4]_{obs}$-poor surface with UCDW (Figure S3 in Supporting Information S1).

3.2. Model Results

3.2.1. Modeled Silicic Acid and $\delta^{30}Si$ Distributions

The large-scale meridional structures of modeled $[Si(OH)_4]$ and $\delta^{30}Si$ along the transect are plotted in Figure 4. Comparison of Figures 2a, 2c, and 4 shows that the model captures most of the key large-scale features observed along $GP17_{OCE}$, including the light $\delta^{30}Si$ of the deep SO, the heavy $\delta^{30}Si$ in SAMW and AAIW into the South Pacific basin, and the southward inflow of deep PDW at the northern end of the $GP17_{OCE}$ transect. To summarize the regional contributions of preformed and regenerated $[Si(OH)_4]$ and their $\delta^{30}Si$ fields to key water masses, we divide the global ocean surface into four regions: (a) the global ocean north of the SAZ, (b) the outcropping regions of both SAMW in the SAZ and (c) AAIW in the PFZ, and (d) the polar SO (Section 2.4).

The modeled preformed $[Si(OH)_4]_{pre}$ and regenerated $[Si(OH)_4]_{reg}$ fields (regardless of surface origin, i.e., "total") along $GP17_{OCE}$ are shown in Figures 5a and 5b, respectively. The regenerated pool generally has much higher $[Si(OH)_4]$ than the preformed pool. The contribution from the regenerated pool generally increases with depth and represents ≥50% of total $[Si(OH)_4]$ in all water masses denser than SAMW. Within AABW and PDW, regenerated silicic acid contributes 75% and 80% of the total $[Si(OH)_4]$, respectively (Figure 5b). The contributions from each surface region to total $[Si(OH)_4]_{pre}$ and total $[Si(OH)_4]_{reg}$ are shown in the left and right columns of Figure 5, respectively. Preformed $[Si(OH)_4]_{pre}$ increases with depth and is dominated by the contribution from the polar SO south of the Antarctic divergence, where weak Si uptake in surface waters allows the subduction of an appreciable preformed pool (Figure 5j). In contrast, north of the divergence, $Si(OH)_4$ drawdown during the northward Ekman flow toward the SAMW (Figure 5e) and AAIW (Figure 5g) outcrop regions results in low $[Si(OH)_4]_{pre}$ being subducted with mode and intermediate waters, with virtually no contributions to other water masses from these outcrops. The global ocean north of the SAZ contributes very little $[Si(OH)_4]_{pre}$ anywhere along the transect (Figure 5c).

For regenerated $Si(OH)_4$ in deep waters, the polar SO is not the dominant source in the model. For AABW, $[Si(OH)_4]_{reg}$ sourced from the polar SO (Figure 5k), the SAMW outcrop (Figure 5i), and the global ocean north of the SAZ (Figure 5d) all contribute similar amounts of $[Si(OH)_4]_{reg}$. Additional inputs of $[Si(OH)_4]_{reg}$ to AABW come from the AAIW outcropping region (Figure 5i), which makes the largest contribution (45%) to total $[Si(OH)_4]$ in AABW. In the deep waters of the South Pacific gyre, the SAMW (Figure 5f) and AAIW (Figure 5i) outcropping regions contribute modest amounts of $[Si(OH)_4]_{reg}$, while the global ocean north of the SAZ contributes the majority of $[Si(OH)_4]_{reg}$ to the mid-depth waters between roughly 40°–20°S (Figure 5d), collocated with the inflow of PDW observed in this region (Section 2.1; Talley et al., 2011).

To understand the sources contributing to $\delta^{30}Si_{obs}$ across the transect, we investigate regional contributions to the total modeled $\delta^{30}Si$ (Figure 4b) from both the preformed (Figure 6) and regenerated (Figure 7) $Si(OH)_4$ pools. Figure 6 shows the contribution from each of the four surface-origin regions (Section 2.4) to $\delta^{30}Si_{pre}$. Magenta lines demarcate the surface-origin regions and correspond to the isopycnal bounds of SAMW and AAIW. For a given region, the contribution to $\delta^{30}Si_{pre}$ is determined by (a) the fraction f_{pre} of total $[Si(OH)_4]_{pre}$ contributed from the region (first column) and (b) the $\delta^{30}Si_{pre}$ value of the preformed $Si(OH)_4$ sourced from the region (second column, referred to as "regionally sourced" below). The contribution from a given region to the total $\delta^{30}Si_{pre}$ value is determined by the product $f_{pre} \times \delta^{30}Si_{pre}$ (third column; Holzer & Brzezinski, 2015), with the total $\delta^{30}Si_{pre}$, being the sum of the products over all regions covering the global ocean (Figure 6m). The contribution of heavy $\delta^{30}Si_{pre}$ in the third column may therefore result from different mechanisms. For example, the polar SO region makes a large fractional contribution to $[Si(OH)_4]_{pre}$ at depth (Figure 6j) that has a light isotopic composition (Figure 6k), resulting in an overall large $\delta^{30}Si_{pre}$ in bottom waters (Figure 6l). Note that the polar SO is the only significant contributor of $[Si(OH)_4]_{pre}$ to deep SO deep waters (Figure 6j), which therefore have an

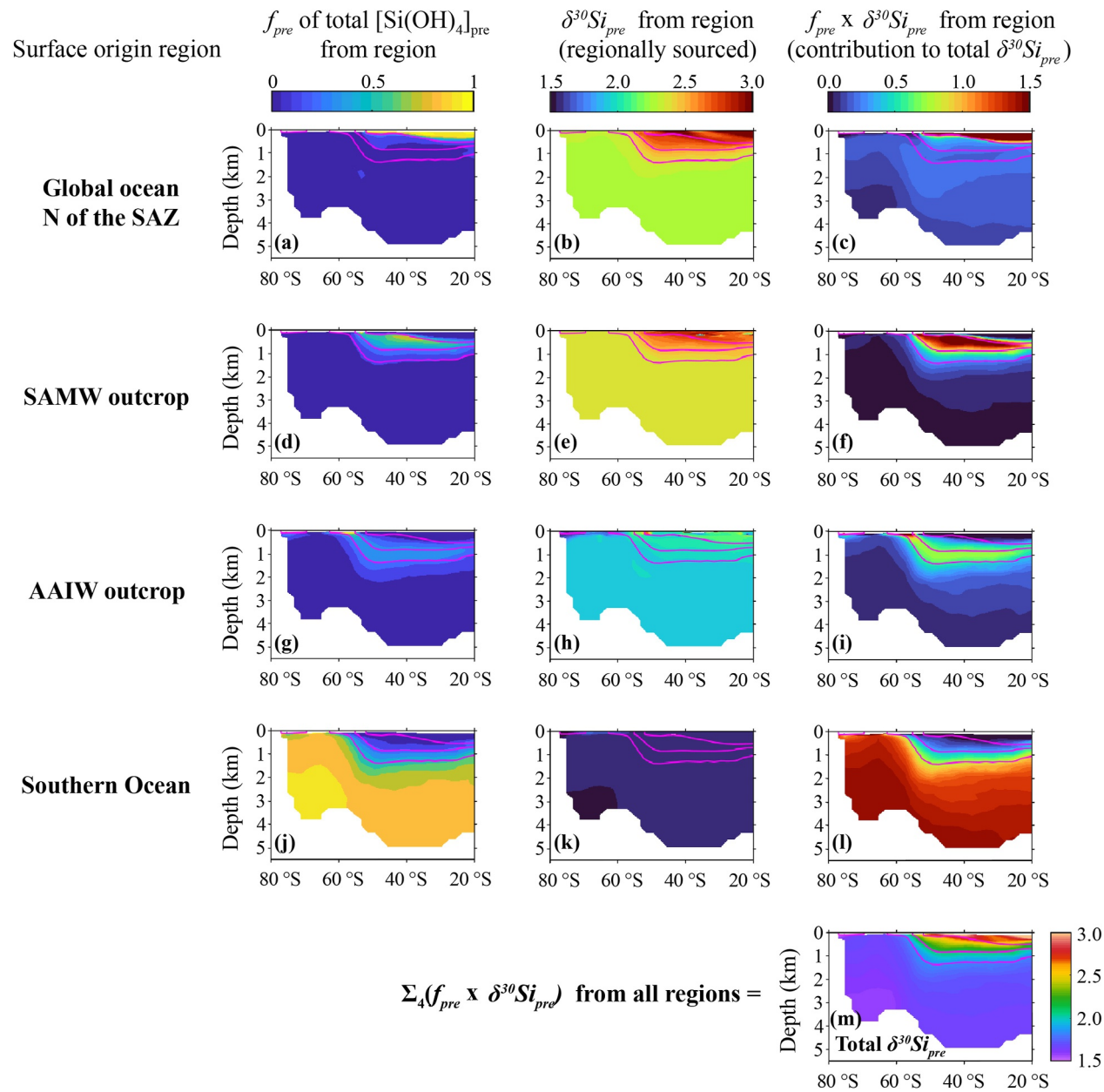


Figure 6. Model results for the $\delta^{30}Si$ of preformed $Si(OH)_4$ sourced from each of the four surface origin regions defined in Section 2.4 and the contribution of this partitioned isotope signature to the $\delta^{30}Si$ of total preformed $Si(OH)_4$ regardless of surface origin. The left column (a, d, g, and j) shows the local, point-wise fraction f_{pre} from each region of total preformed $Si(OH)_4$, while the middle column (b, e, h, and k) shows the $\delta^{30}S_{pre}$ of preformed $Si(OH)_4$ sourced from the respective region (i.e., regionally sourced). The right column (e, f, i, and l) shows the contribution to the total preformed $\delta^{30}Si_{pre}$ from a given region, which is the product of f_{pre} and $\delta^{30}Si_{pre}$. Color scales for a–l are located above each column. The $\delta^{30}Si_{pre}$ (of the total preformed $Si(OH)_4$) along the transect (*m*) is the sum of the contributions from all four origin regions with the associated color scale to the right.

isotopically light total $\delta^{30}Si_{pre}$ (Figure 6m). In contrast, the heavy $\delta^{30}Si_{pre}$ contribution to SAMW (Figure 6f) and AAIW (Figure 6i) from their outcrop regions results from a modest fractional contributions to total $[Si(OH)_4]_{pre}$ (Figures 6d and 6g) but with heavy regionally sourced $\delta^{30}Si_{pre}$ (Figures 6e and 6h). While both mode and intermediate waters receive heavy contributions to total $\delta^{30}Si_{pre}$, the contribution to SAMW is substantially heavier than that to AAIW. This difference results from SAMW receiving both a greater fractional contribution to $[Si(OH)_4]_{pre}$ (Figure 6d) and a heavier regionally sourced $\delta^{30}Si_{pre}$ (Figure 6e) compared to AAIW (Figures 6g and 6h).

19449224, 2026, 5, Downloaded from https://agupubs.onlinelibrary.wiley.com/doi/10.1029/2025GB009008 by Finnish Meteorological, Wiley Online Library on [29/09/2026]. See the Terms and Conditions (https://onlinelibrary.wiley.com/terms-and-conditions) on Wiley Online Library for rules of use; OA articles are governed by the applicable Creative Commons License

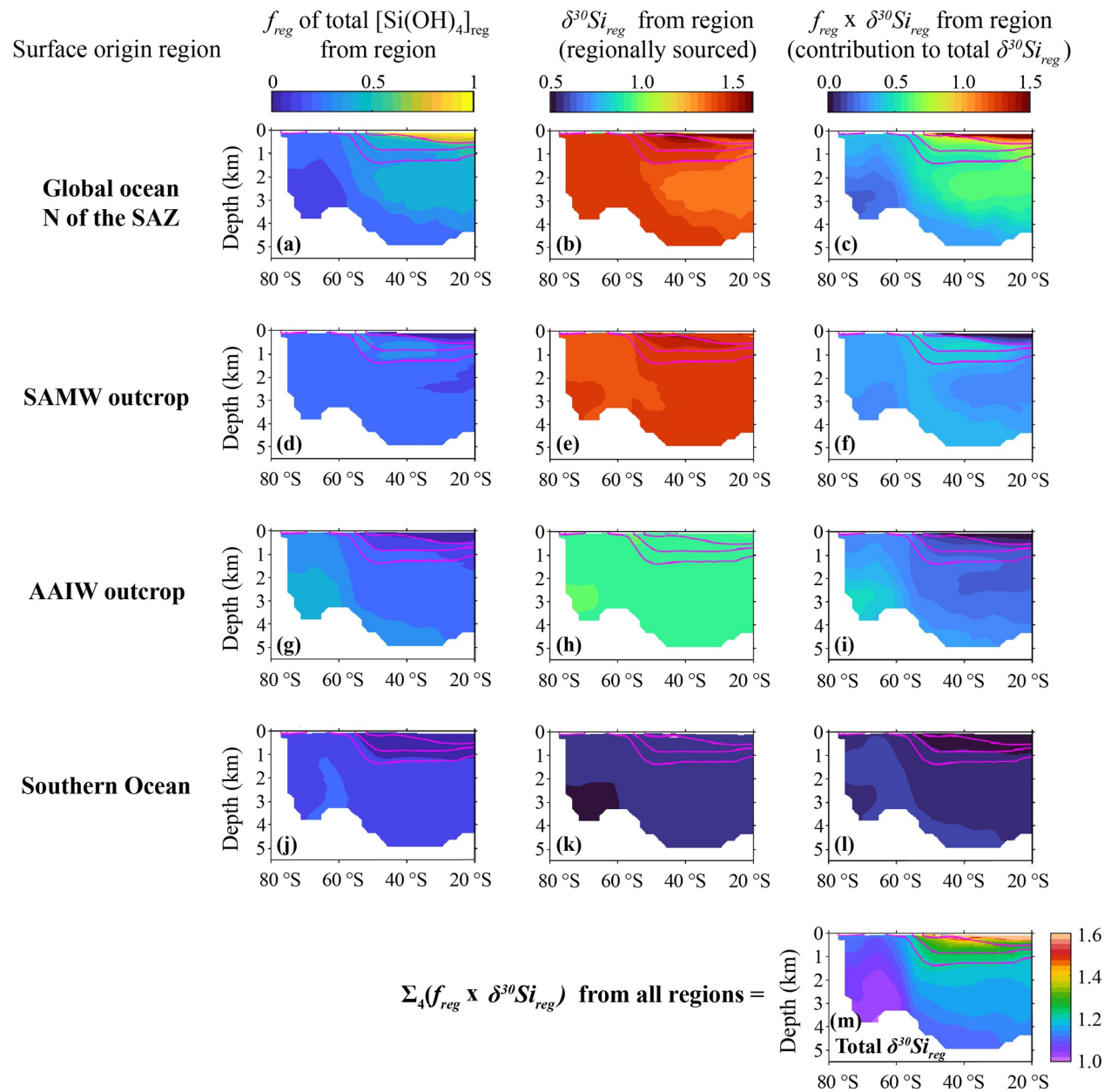


Figure 7. As Figure 6, but for the $\delta^{30}Si_{reg}$ of regenerated $Si(OH)_4$.

The heavy $\delta^{30}Si_{pre}$ contributions from the mode and intermediate water outcropping regions predominantly spread along isopycnals within these water masses along the $GP17_{OCE}$ transect, extending northward to 20°S with little variation along the isopycnals (Figures 6f and 7f). The heavy $\delta^{30}Si_{pre}$ of both SAMW (Figure 6f) and AAIW (Figure 6i) diffuse vertically above and below the subducted water masses, while the heavy $\delta^{30}Si_{pre}$ contribution of the deep waters sourced from the polar SO diffuses up into both SAMW and AAIW (Figure 6l). Modeled upper-ocean waters above SAMW have a high fractional contribution of $[Si(OH)_4]_{pre}$ from the global ocean north of the SAZ (Figure 6a) with a very heavy regionally sourced isotopic composition (Figure 6b), producing the heaviest contribution to $\delta^{30}Si_{pre}$ within the upper South Pacific gyre (Figure 6c). However, while this region makes a high fractional contribution to the total $[Si(OH)_4]_{pre}$, $[Si(OH)_4]_{pre}$ itself contributes a vanishingly small amount to total $[Si(OH)_4]$ in the region (Figure 5a) and therefore has only a minor effect on the total $\delta^{30}Si$. Within the preformed pool, very low fractional contributions to total $[Si(OH)_4]_{pre}$ from all regions north of the polar SO

19449224, 2026, 5, Downloaded from https://agupubs.onlinelibrary.wiley.com/doi/10.1029/2025GB009008 by Finnish Meteorological, Wiley Online Library on [29/09/2026]. See the Terms and Conditions (https://onlinelibrary.wiley.com/terms-and-conditions) on Wiley Online Library for rules of use; OA articles are governed by the applicable Creative Commons License

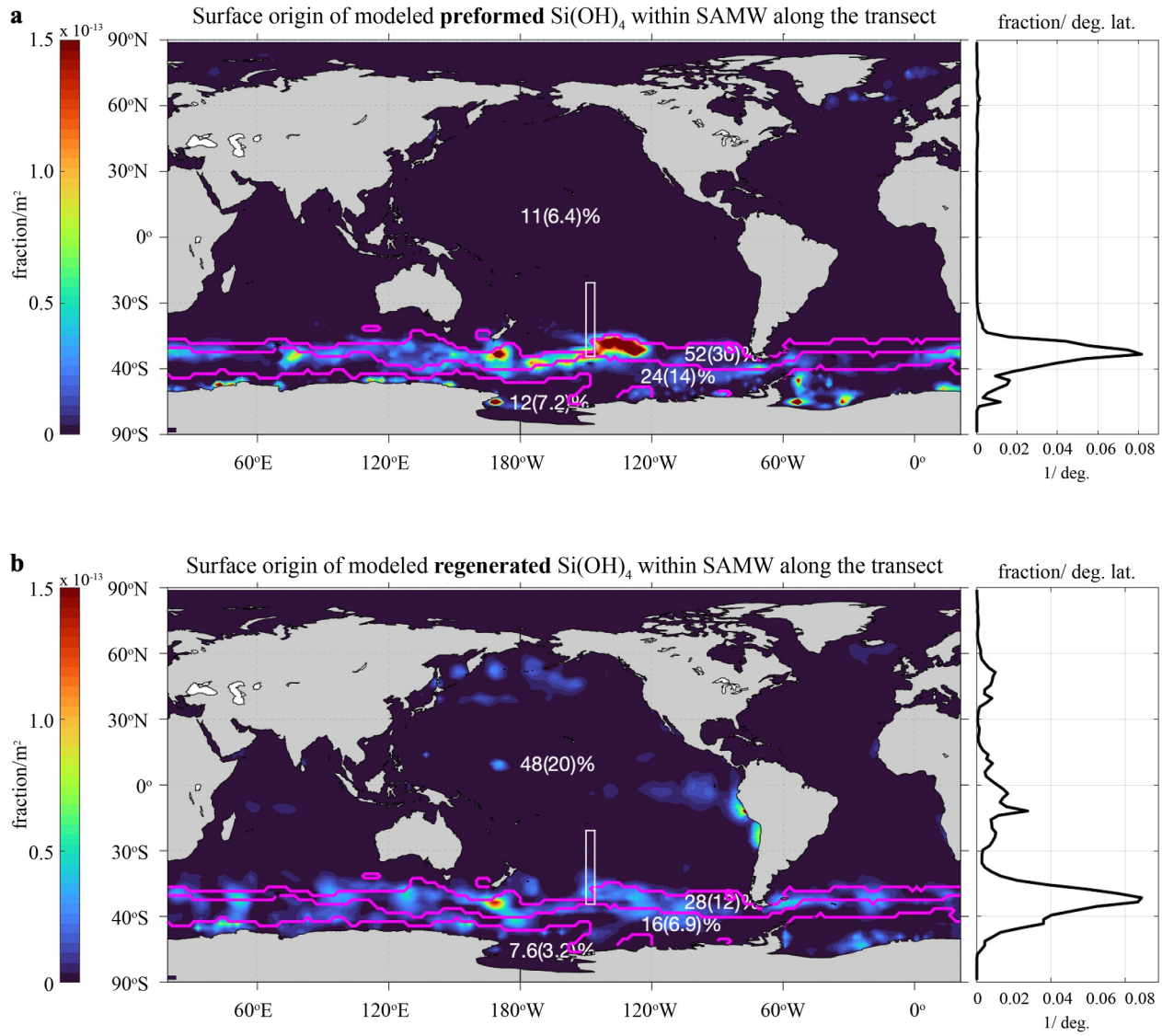


Figure 8. (a) Map of the fractional surface-origin contribution per unit area to the $[Si(OH)_4]_{pre}$ contained in the Sub-Antarctic Mode Water (SAMW) sub-volume between potential densities $26.80 \leq \sigma_\theta \leq 27.06$ kg m^{-3} along $GP17_{OCE}$ between 60°–20°S and 146°–150°W (indicated by the white box). (The global area integral of this map gives unity in accord with the units of the color bar.) The magenta lines demarcate the four surface-origin regions discussed in Figures 5–7 and defined in Section 2.4. Percentages shown in white on the figure are the % contribution of that surface-origin region to the preformed $[Si(OH)_4]_{pre}$ in the SAMW sub-volume, while bracketed percentages are the % contribution to total $[Si(OH)_4]$ in the SAMW sub-volume. The white percentages are thus area integrals of the map over the regions bounded by the magenta lines. (b) Same as (a) but for regenerated $[Si(OH)_4]$ within the SAMW sub-volume. The zonal integrals of the maps are shown to the right.

(Figures 6a, 6d, and 6g), and a very high fractional contribution (Figure 6j) of light $\delta^{30}Si_{pre}$ originating in the polar SO (Figure 6k) lead to a minimum in total $\delta^{30}Si_{pre}$ within deep polar AABW (Figure 6m).

Focusing on modeled $[Si(OH)_4]_{reg}$ and its $\delta^{30}Si_{reg}$, Figure 7 shows very different regional contributions to mode/intermediate waters and AABW than those just discussed for the preformed pool. When considering the fractional contribution of each region to the total $[Si(OH)_4]_{reg}$, it is important to keep in mind that regenerated $Si(OH)_4$ represents more than 50% of total $[Si(OH)_4]$ in all water masses denser than SAMW (Figure 5b) and therefore strongly influences the total modeled isotopic composition of deep waters. The polar SO makes a relatively small fractional contribution (Figure 7j) that carries a very light regionally sourced $\delta^{30}Si_{reg}$ (Figure 7k) for an overall isotopically very light contribution to total $[Si(OH)_4]_{reg}$ in deep waters (Figure 7l).

Unlike in the preformed pool, the contributions to $\delta^{30}Si_{reg}$ from the SAMW (Figure 7f) and AAIW (Figure 7i) outcrop regions differ significantly. The AAIW outcrop delivers the highest fractional contribution to the total [Si

19449224, 2026, 5, Downloaded from https://agupubs.onlinelibrary.wiley.com/doi/10.1029/2025GB009008 by Finnish Meteorological, Wiley Online Library on [29/09/2026]. See the Terms and Conditions (https://onlinelibrary.wiley.com/terms-and-conditions) on Wiley Online Library for rules of use; OA articles are governed by the applicable Creative Commons License

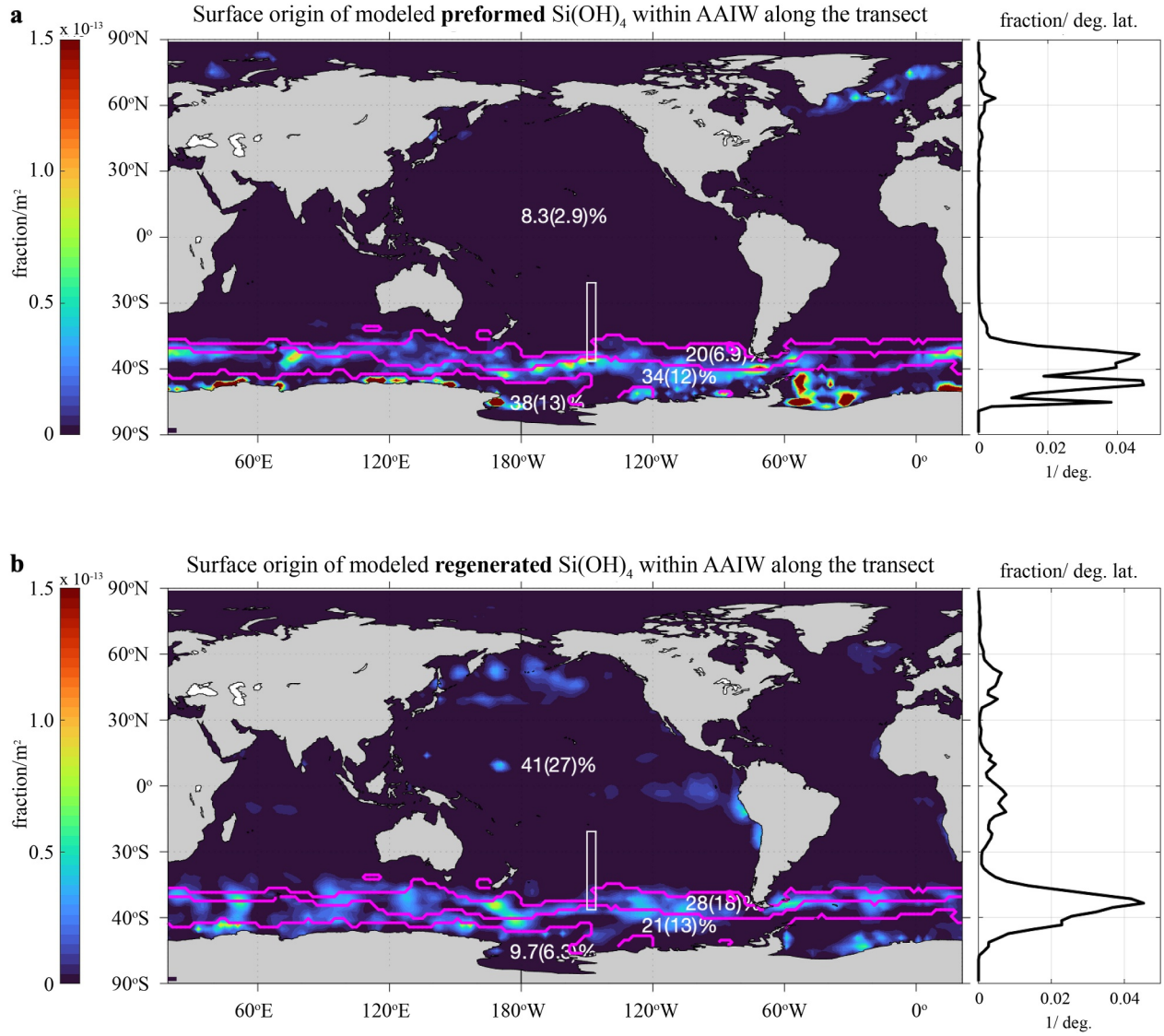


Figure 9. As Figure 8, but for the Antarctic Intermediate Water sub-volume between potential densities $27.06 \leq \sigma_\theta \leq 27.4$ kg m^{-3} along GP17$_{OCE}$ between 60°–20°S and 146°–150°W (indicated by white box). (The global area integral of this map again gives unity in accord with the units of the color bar.)

$(OH)_4]_{reg}$ in AABW (Figure 7g) with a relatively light regionally sourced isotopic composition (~+1‰; Figure 7h). The high fractional contribution from the AAIW outcrop to total $[Si(OH)_4]_{reg}$ in AABW makes the heaviest contribution to $\delta^{30}Si_{reg}$, although this contribution remains relatively light (Figure 7i). The AAIW outcrop region does not contribute a substantial fraction of $[Si(OH)_4]_{reg}$ to AAIW, leading to a minimal contribution to $\delta^{30}Si_{reg}$ within AAIW itself (Figure 7i). By contrast, while SAMW receives only a slightly higher fraction of $[Si(OH)_4]_{reg}$ from its outcropping region (Figure 7d), the very heavy isotopic composition sourced from the SAMW outcrop (Figure 7e) leads to an overall contribution of relatively heavy $\delta^{30}Si_{reg}$ within SAMW (Figure 7f). Neither the SAMW (Figure 7d) nor the AAIW (Figure 7g) outcrop region contribute significantly to the mid-depth waters at the northern end of the transect (20°S), leading to isotopically light contributions to $\delta^{30}Si_{reg}$ at mid depth (Figures 7f and 7i, respectively). The same mid-depth waters receive high fractional inputs to total $[Si(OH)_4]_{reg}$ sourced from the global ocean north of the SAZ (Figure 7a), which also contributes a large fraction of the total $[Si(OH)_4]_{reg}$ in the upper South Pacific gyre. The isotopic composition sourced from the global ocean north of the SAZ is overwhelmingly heavy across the transect (Figure 7b). The silicic-acid fraction and $\delta^{30}Si_{reg}$ sourced from this region have a broadly similar structure, which is then also reflected in their product, which is the contribution to total $\delta^{30}Si_{reg}$ (Figure 7c).

19449224, 2026, 5, Downloaded from https://agupubs.onlinelibrary.wiley.com/doi/10.1029/2025GB009008 by Finnish Meteorological, Wiley Online Library on [29/09/2026]. See the Terms and Conditions (https://onlinelibrary.wiley.com/terms-and-conditions) on Wiley Online Library for rules of use; OA articles are governed by the applicable Creative Commons License

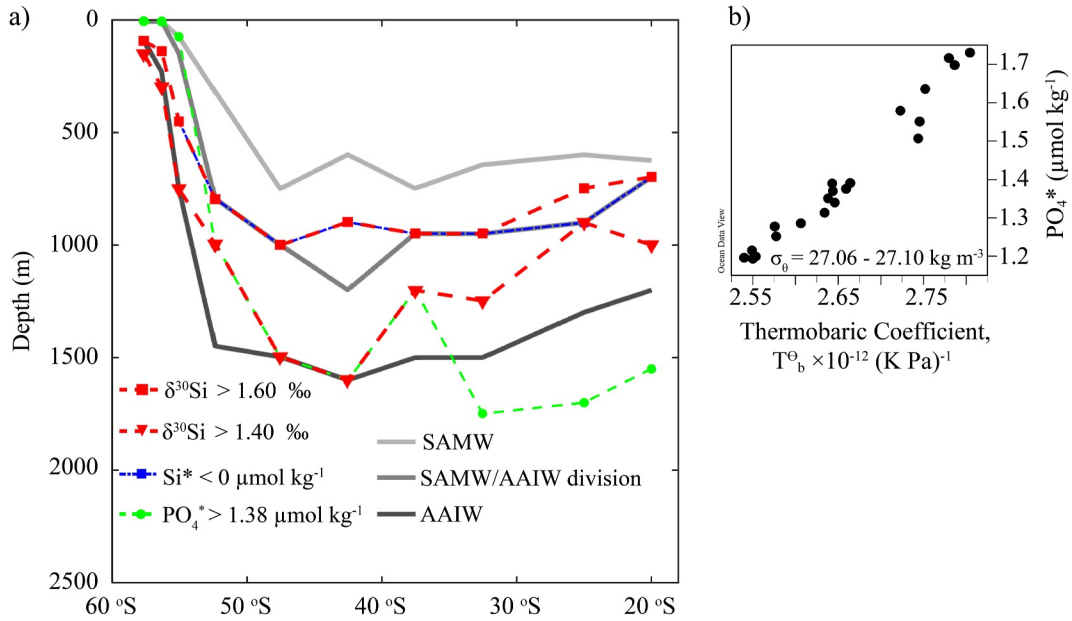


Figure 10. (a) A comparison of the maximum depths of elevated $\delta^{30}Si_{obs}$ within Sub-Antarctic Mode Water (SAMW) (26.9 kg m^{-3} < σ_θ < 27.06 kg m^{-3}) and Antarctic Intermediate Water (AAIW) (27.06 kg m^{-3} < σ_θ < 27.10 kg m^{-3}) along the $GP17_{OCE}$ meridional transect. Within SAMW, the maximum depth of elevated $\delta^{30}Si_{obs}$ > 1.6‰ and maximum depth of negative Si* (Sarmiento et al., 2004) show strong coherence, suggesting shared hydrographic controls. Within AAIW, elevated $\delta^{30}Si_{obs}$ > 1.40‰ and elevated PO_4* > 1.38 µmol kg^{-1} have maximum depths with similar latitude dependence. Note that the Si* < 0 µmol kg^{-1} line (blue dash) is overlapped by the $\delta^{30}Si$ > 1.40‰ line. In (b), the strong correlation between the thermobaric coefficient (a metric of non-linear mixing) and PO_4*, suggests that the diapycnal mixing of AAIW and UCDW plays a role in setting the elevated $\delta^{30}Si_{obs}$ of AAIW (Section 4.1).

3.2.2. Surface Origin Maps of Preformed and Regenerated Silicic Acid in Mode Waters

The model provides additional insight into the $\delta^{30}Si_{pre}$ and $\delta^{30}Si_{reg}$ distributions along the $GP17_{OCE}$ by allowing us to trace the interior silicon pools to their geographic origin in the euphotic zone. Figures 8 and 9 show the local contributions per unit surface area of both preformed and regenerated $Si(OH)_4$ within the modeled SAMW and AAIW sub-volumes along $GP17_{OCE}$ (Section 2.4). The surface origin was calculated using an adjoint method (e.g., Brzezinski et al., 2025; Holzer et al., 2021) to trace preformed $Si(OH)_4$ contained within these interior water masses back to where it was last ventilated (Figures 8a and 9a) and regenerated $Si(OH)_4$ back to where it was last exported as biogenic opal from the euphotic zone (Figures 8b and 9b). Surface origin maps were normalized by the total amount of either preformed or regenerated silicic acid in the sub-volume so that its global surface integral of the maps gives unity. To guide the eye, magenta lines in Figures 8 and 9 demarcate the density-based regional partitions used in Figures 5–7. For ease of comparison, differences in the surface origin of preformed $Si(OH)_4$ in the SAMW and AAIW sub-volumes will be described together, followed by a description of the surface origin of regenerated $Si(OH)_4$.

Preformed $Si(OH)_4$ contributes 57.6% of total $[Si(OH)_4]$ within the SAMW sub-volume. Of the preformed fraction, 52% (30% of total $[Si(OH)_4]$ in the sub-volume) originates from the SAMW outcrop itself (Figure 8a). Preformed $Si(OH)_4$ delivered to SAMW from its outcrop is largely sourced from along the Pacific Antarctic Ridge just to the east of 146°–150°W and from south of Aotearoa (New Zealand) in the region of the Campbell Plateau. The AAIW outcrop contributes 24% of $[Si(OH)_4]_{pre}$ in the SAMW sub-volume, while 12% of $[Si(OH)_4]_{pre}$ originates in the polar SO. Most of the $[Si(OH)_4]_{pre}$ originating in the polar SO comes from known deep-water formation regions in the Ross and Weddell Seas (Figure 8a). The global ocean north of the SAZ contributes only 11% of $[Si(OH)_4]_{pre}$ in the SAMW sub-volume, with the majority of this contribution coming from the deep-water formation regions of the North Atlantic (Talley et al., 2011).

Within the AAIW sub-volume, $[Si(OH)_4]_{pre}$ accounts for only 34.8% of total $[Si(OH)_4]$, with the three high-southern-latitude regions contributing 92% of this fraction (31.9% of total $[Si(OH)_4]$; Figure 9a). Within these

19449224, 2026, 5, Downloaded from https://agupubs.onlinelibrary.wiley.com/doi/10.1029/2025GB009008 by Finnish Meteorological, Wiley Online Library on [29/09/2026]. See the Terms and Conditions (https://onlinelibrary.wiley.com/terms-and-conditions) on Wiley Online Library for rules of use; OA articles are governed by the applicable Creative Commons License

19449224, 2026, 5, Downloaded from https://agupubs.onlinelibrary.wiley.com/doi/10.1029/2025GB009008 by Finnish Meteorological, Wiley Online Library on [29/09/2026]. See the Terms and Conditions (https://onlinelibrary.wiley.com/terms-and-conditions) on Wiley Online Library for rules of use; OA articles are governed by the applicable Creative Commons License

regions, the preformed contribution decreases moving northward, as expected from progressively increasing nutrient consumption, with $Si(OH)_4$ originating in the polar SO, AAIW outcrop, and SAMW outcrop contributing 38%, 34%, and 20%, respectively. Much of the $[Si(OH)_4]_{pre}$ sourced from these surface regions originated along the Pacific-Antarctic Ridge to the west of 146°–150°W, in the AAIW formation region in the Drake Passage (Bostock et al., 2013), and in polar deep-water formation regions (Figure 9a; Talley et al., 2011). Similar to SAMW, the deep-water formation regions of the North Atlantic and Nordic Seas are prominent contributors to the remaining 8.3% of $[Si(OH)_4]_{pre}$ originating north of the SAZ.

Regenerated $Si(OH)_4$ in the SAMW and AAIW sub-volumes show marked differences in their surface origin compared to the preformed pools in these sub-volumes. While $[Si(OH)_4]_{pre}$ in the SAMW sub-volume is largely sourced from the SAMW outcrop, 48% of $[Si(OH)_4]_{reg}$ (20% of total $[Si(OH)_4]$) comes from the global ocean north of this outcrop (Figure 8b). The fraction of northern-sourced $[Si(OH)_4]_{reg}$ increases moving north, particularly at the depths of southward flowing PDW (Figure 5d), with much of this fraction last utilized in the North Pacific and Eastern Equatorial Pacific (Figure 8b). As expected, very little regenerated $Si(OH)_4$ traces back to the oligotrophic gyres, including minimal regenerated sources between 20° and 35°S along $GP17_{OCE}$ (Figure 8b). In high southern latitudes, the origin of $[Si(OH)_4]_{reg}$ in the SAMW sub-volume diminishes southward, with the SAMW outcrop, AAIW outcrop, and the polar SO contributing 28%, 16%, and 7.6% of $[Si(OH)_4]_{reg}$, respectively. The largest regenerated contributions in the high southern latitudes lie to the south Aotearoa (New Zealand) above the productive Campbell Plateau (Figure 8b; Gutiérrez-Rodríguez et al., 2023), in agreement with the pattern of biological silicic-acid uptake (Holzer et al., 2014).

Within the AAIW sub-volume, $[Si(OH)_4]_{reg}$ contributes 64% of total $[Si(OH)_4]$ (Figure 9b). In high southern latitudes, contributions to $[Si(OH)_4]_{reg}$ within the AAIW sub-volume also decrease moving southward with the SAMW outcrop, AAIW outcrop, and polar SO contributing 28%, 21%, and 9.7%, respectively. Similar to the SAMW sub-volume, nearly half (41%) of $[Si(OH)_4]_{reg}$ in the AAIW sub-volume originates north of the SAZ. Northern-sourced $[Si(OH)]_{reg}$ in AAIW shows similar surface-origin contributions as $[Si(OH)_4]_{reg}$ in SAMW, mirroring global silicic-acid uptake patterns (Figure 9b; Holzer et al., 2014). Distal sources of $[Si(OH)_4]_{reg}$ strongly influence the signature of the SAMW and AAIW sub-volumes along the $GP17_{OCE}$ meridional transect, with very little of the $[Si(OH)_4]_{reg}$ tracing back to the overlying South Pacific gyre (Figures 8b and 9b).

4. Discussion

The combination of biological silicon isotope fractionation in surface waters, mode and intermediate water transport, and high-latitude nutrient trapping controls much of the $[Si(OH)_4]_{obs}$ and $\delta^{30}Si_{obs}$ distributions along the $GP17_{OCE}$ transect (Figure 1a). Our analyses show that the combination of these physical and biogeochemical drivers produces two distinct features also seen in global models: isotopically heavy, $[Si(OH)_4]$-poor mode/intermediate waters and isotopically light, $[Si(OH)_4]$-rich SO deep waters. Furthermore, improved analytical precision reveals hydrographically consistent latitudinal and depth-dependent patterns in deep waters along the meridional transect (Figure 2c). Below, we discuss model and data-based results which illuminate the role of preformed and regenerated $Si(OH)_4$ in modulating the silicon isotope dynamics of mode and deep waters and the role of diapycnal mixing along the MOC in distributing these signatures northward to the low-latitude South Pacific.

4.1. Processes Leading to Heavy $\delta^{30}Si_{obs}$ in SAMW and AAIW

Our model indicates strong isopycnal control on the heavy $\delta^{30}Si_{obs}$ of mode and intermediate waters. The relationship between elevated $\delta^{30}Si_{obs}$ and mode-water subduction was quantitatively assessed through comparison between the deepest surface of elevated $\delta^{30}Si_{obs}$ (>+1.6‰), the deepest extent of negative Si*, and the spreading densities of SAMW (26.9 kg m^{-3} < σ_θ < 27.06 kg m^{-3}) along the transect (de Souza, Reynolds, Johnson, et al., 2012). Elevated $\delta^{30}Si_{obs}$ and negative Si* are formed via the drawdown of $Si(OH)_4$ by diatoms in the iron-limited surface of the high southern latitudes (Closset et al., 2016; Sarmiento et al., 2004; Varela et al., 2004). Strong agreement between the depths of all three properties was observed, suggesting substantial isopycnal control of mode-water $\delta^{30}Si_{obs}$ during subduction and northward transport (Figure 10a; de Souza, Reynolds, Rickli, et al., 2012). This agrees well with model results indicating a large source of heavy $\delta^{30}Si_{pre}$ (Figure 6f) and an additional minor source of heavy $\delta^{30}Si_{reg}$ (Figure 7f) to the SAMW sub-volume from the SAMW outcropping region, resulting in a total modeled $\delta^{30}Si$ distribution with similar variations within the mode

19449224, 2026, 5, Downloaded from https://agupubs.onlinelibrary.wiley.com/doi/10.1029/2025GB009008 by Finnish Meteorological, Wiley Online Library on [29/09/2026]. See the Terms and Conditions (https://onlinelibrary.wiley.com/terms-and-conditions) on Wiley Online Library for rules of use; OA articles are governed by the applicable Creative Commons License

and intermediate waters (Figure 4b). The coherence of negative Si and elevated $\delta^{30}Si_{obs}$ with the spreading isopycnals of SAMW agrees well with the findings of de Souza, Reynolds, Rickli, et al. (2012), who observed similar isopycnal coherence within SAMW along 103°W between 10° and 60°S in the Atlantic.

Within intermediate waters, enrichment of $\delta^{30}Si_{obs} > +1.4‰$ follows the isopycnals of AAIW ($27.06\ kg\ m^{-3} < \sigma_\theta < 27.10\ kg\ m^{-3}$; Figure 10a). Model results suggest that some of this heavy signature is sourced from preformed $Si(OH)_4$ originating from the surface of the AAIW outcrop (Figure 6i). Notably, the AAIW does not receive similarly heavy $\delta^{30}Si_{reg}$ from its outcrop region (Figure 7i), as the outcrop (27.06–27.4 kg m^{-3}) encompasses portions of the surface ocean where incomplete biological drawdown of $Si(OH)_4$, synonymous with a low degree of $Si(OH)_4$ consumption, results in the export of light $\delta^{30}Si$ in sinking opal (Varela et al., 2004). The AAIW outcropping region encompasses a gradient from $Si(OH)_4$-replete regions toward its southern boundary (27.4 kg m^{-3}, >100 m) to more $Si(OH)_4$-limited regions, that is, where there is a greater degree of $Si(OH)_4$ consumption, toward the northern boundary (27.06 kg m^{-3}; Figure 4a). As such, the regenerated contribution from the AAIW outcropping region (Figure 7h) has an isotopic signature falling between the very light $\delta^{30}Si_{reg}$ sourced from the $Si(OH)_4$-replete polar SO (Figure 7k) and the increasingly $Si(OH)_4$-limited SAMW outcropping region (Figure 7e). This agrees with previous observations in the region, which found monotonically decreasing $\delta^{30}Si_{obs}$ in opal progressing from 60° to 67°S (Varela et al., 2004). Heavy $\delta^{30}Si_{obs}$ in the dissolved phase have been reported previously in SAMW and AAIW outcropping regions and results from high diatom productivity (Cardinal et al., 2005; de Souza, Reynolds, Johnson, et al., 2012; Fripiat et al., 2011; Varela et al., 2004). Within both SAMW and AAIW, heavy isotopic signatures are maintained across the meridional transect, with only minor variation $\delta^{30}Si_{obs}$ between S18 on the PF to at least the northernmost station at 20°S (Figure 10a).

We used our model to quantify the surface origin of $\delta^{30}Si_{pre}$ and $\delta^{30}Si_{reg}$ to better understand controls on the relatively constant, heavy $\delta^{30}Si_{obs}$ of mode and intermediate waters across the meridional transect with the goal of determining the relative contributions from both local and distal sources to $Si(OH)_4$ and $\delta^{30}Si$ in SAMW and AAIW. Constraints on distal sources are particularly important as SAMW and AAIW are often conceptualized as effectively closed conduits which transport water from the surface of the high southern latitudes to the ocean interior with limited interactions with surrounding water masses. Distal sources outside the outcropping regions have the potential to introduce substantial bias into estimates of biogeochemical transformations during SAMW and AAIW transport, including estimates of carbon sequestration along these flow paths (Jutras et al., 2025). Our diagnostics capture the net effect due to all possible modeled advective-eddy-diffusive transport paths and highlight vertical diffusion of heavy $\delta^{30}Si_{pre}$ outward from both SAMW and AAIW, indicating mixing of these water masses (Figures 6f and 6i). Similarly, diapycnal mixing of heavy $\delta^{30}Si_{pre}$ in UCDW from distal sources in the polar SO into less dense AAIW, and to a lesser extent SAMW, is evident along $GP17_{OCE}$ (Figure 6l) and consistent with previous hydrographic work that identified diapycnal mixing of these water masses (Li et al., 2021, 2022). In our model, mixing with UCDW leads to a large fractional contribution from the polar SO to $[Si(OH)_4]_{pre}$ within AAIW (Figure 6j). This results in AAIW with heavy total $\delta^{30}Si_{pre}$ made up about equally from heavy $\delta^{30}Si_{pre}$ subducted in the AAIW outcrop (34%) and heavy $\delta^{30}Si_{pre}$ entrained from underlying UCDW (38%, Figure 9a).

Model results suggest that diapycnal mixing of AAIW with the top of UCDW entrains heavy $\delta^{30}Si_{pre}$ sourced from the polar SO (Section 3.2.1, Figures 5k and 6l). We assess UCDW entrainment into AAIW in the observed data through the examination of the depth of the shallowest surface of elevated $PO_4^* = [PO_4^{3-}] + [O_2]/175–1.95$ (Broecker et al., 1991) in relation to the depth of the deepest surface of elevated $\delta^{30}Si_{obs}$ within AAIW (Figure 10a). Across the transect, PO_4^* generally increases with depth (Figure S1d in Supporting Information S1), as respiration draws down oxygen and releases inorganic PO_4^{3-} from organic matter. Along the outflow of the AAIW, there is very little new organic matter input from the surface of the oligotrophic gyre (Figure 9b). Thus, following the subduction of AAIW, elevated PO_4^* is associated with deep waters along the outflow of AAIW and variations along this path at depth are indicative of deep-water entrainment (Carter et al., 2014). The coherence of the shallowest surface of elevated PO_4^* with the deepest surface of elevated $\delta^{30}Si_{obs}$ suggests that entrainment of UCDW impacts $\delta^{30}Si_{obs}$ within AAIW (Figure 10a). To further assess this potential entrainment signature, we consider nonlinear water-mass mixing related to variation in the thermal expansion coefficient, known as thermobaricity (T^{θ}_{b}; Kay, 2001). At depth, greater values of T^{θ}_{b} indicate higher potential for diapycnal mixing through a positive buoyancy flux (McDougall, 1987). Along the transect within AAIW, increasing T^{θ}_{b} is associated with increasing PO_4^* (Figure 10b), further indicating the likelihood of entrainment of PO_4^*-rich UCDW into AAIW. In the northern end of the transect between 20° and 40°S, the divergence of $\delta^{30}Si_{obs}$ from PO_4^* is likely driven by entrainment of isotopically heavy $\delta^{30}Si_{reg}$ sourced from the global ocean north of the SAZ

19449224, 2026, 5, Downloaded from https://agupubs.onlinelibrary.wiley.com/doi/10.1029/2025GB009008 by Finnish Meteorological, Wiley Online Library on [29/09/2026]. See the Terms and Conditions (https://onlinelibrary.wiley.com/terms-and-conditions) on Wiley Online Library for rules of use; OA articles are governed by the applicable Creative Commons License

(Figures 7c and 10b). This inferred entrainment complements our model diagnostics and indicates that diapycnal mixing of UCDW transports heavy $\delta^{30}Si_{pre}$ sourced from the polar SO into AAIW (Figures 5j and 6l). Entrainment of UCDW thus provides a deep-water source of heavy $\delta^{30}Si_{pre}$ to AAIW across the entire transect. The finding of diapycnal mixing of $\delta^{30}Si$ and PO_4^* signatures carried within UCDW into AAIW agrees with previous calculations of AAIW modification through deep-water mixing in the South Pacific (Carter et al., 2014; Jutras et al., 2025; Li et al., 2022).

Our analysis indicates that while there are only minor variations in the $\delta^{30}Si_{obs}$ of mode and intermediate waters between S1 at 20°S and S18 on the PF (56°S), multiple sources contribute to the heavy $\delta^{30}Si_{obs}$ within SAMW and AAIW. These include isotopically heavy fractions of preformed and regenerated silicic acid from both local outcrops and from distal sources. Heavy preformed signatures originate in the high southern latitudes and comprise both heavy $\delta^{30}Si_{pre}$ subducted at the outcrops (Figures 6f and 6i) and heavy $\delta^{30}Si_{pre}$ sourced from the polar SO, which contributes to the $\delta^{30}Si_{pre}$ of SAMW and AAIW through the entrainment of underlying UCDW (Figure 6l). Entrained waters have a nearly uniform isotopic composition across the transect, contributing to the relatively constant $\delta^{30}Si_{pre}$ within mode and intermediate water along isopycnals (Figure 6m). Heavy regenerated $\delta^{30}Si_{reg}$ comes predominantly from distal sources north of the SAZ (Figure 7c), with a minor contribution of heavy $\delta^{30}Si_{reg}$ to SAMW and AAIW from the SAMW outcrop (Figure 7f). Similar to heavy $\delta^{30}Si_{pre}$ entrained from UCDW, heavy $\delta^{30}Si_{reg}$ from distal regions north of the SAZ finds its way into SAMW and AAIW through entrainment of underlying UCDW (Figures 5d and 7c). The combination of these regenerated sources leads to a heavy $\delta^{30}Si_{reg}$ signature within mode and intermediate waters that is approximately constant along isopycnals (Figure 7m). In the model, $\delta^{30}Si$ of the preformed and regenerated silicic acid combine to produce a $\delta^{30}Si$ signature in SAMW and AAIW that is approximately constant along isopycnals (Figure 4b) in good agreement with observations (Figure 2c).

Along $GP17_{OCE}$, a substantial portion of heavy $\delta^{30}Si$ in SAMW and AAIW occurs through entrainment of water isotopically imprinted by distal sources (Figures 8 and 9). These distal signatures are particularly important to constrain, as they introduce bias into estimates of organic respiration, and therefore estimates of carbon sequestration in SAMW and AAIW (Carter et al., 2014). Specifically, it has been suggested that these distal signatures may result in overestimation of organic respiration by more than 50% (Jutras et al., 2025). Our observations and modeling support the importance of distal sources on mode and intermediate waters, with the implication that their influence must be accounted for in accurate estimations of biogeochemical transformations.

4.2. Silicon Trapping in the Southern Ocean

In the deep SO, both measurements (Figure 2c) and model results (Figure 4b) show that accumulation of $[Si(OH)_4]_{reg}$ and the associated light $\delta^{30}Si_{reg}$ drive a minimum in $\delta^{30}Si_{obs}$ in AABW (Figures 5b and 7m). The SO is a well-known region of nutrient trapping, where the circulation returns $[Si(OH)_4]_{reg}$ back to the original surface region of its export (Holzer et al., 2014; Primeau et al., 2013). Models and observations suggest that the consecutive return of $Si(OH)_4$ to the surface of the polar SO amplifies the light signature of $\delta^{30}Si_{reg}$ through repeated uptake and fractionation (Closset et al., 2016; Fripiat et al., 2011; Holzer & Brzezinski, 2015; Varela et al., 2004). Correspondingly, we find that along the $GP17_{OCE}$ $\delta^{30}Si_{obs}$ in the deep polar SO is dominated by the regenerated pool, which contributes 72% of total $[Si(OH)_4]$ (Figure 5b) and has a very light $\delta^{30}Si_{reg}$ signature (~+1.025‰; Figure 7m). The lightest $\delta^{30}Si_{reg}$ contribution to the deep polar SO is sourced from the polar SO itself (Figure 7l), consistent with silicon trapping producing exceptionally light $\delta^{30}Si_{reg}$ in combination with a low degree of nutrient consumption in polar SO surface waters (Figure 7k; Brzezinski et al., 2025; Holzer et al., 2014). The remaining 28% of total $[Si(OH)_4]$ comes from the preformed pool and is almost entirely sourced from the polar SO where AABW forms (Figure 5j). In the SO, $Si(OH)_4$ undergoes incomplete biological utilization due to micronutrient limitation (Sarmiento et al., 2004), which leads to both preformed (Figure 6k) and regenerated (Figure 7k) $\delta^{30}Si$ that is isotopically lighter than that found in all other regions where $Si(OH)_4$ itself is limiting (Figures 6b, 6e, 6h, 7b, 7e, and 7h). Model results and observations thus support the idea that the exceptionally light $\delta^{30}Si_{obs}$ of the deep polar SO is controlled by both repeated fractionation through SO silicon trapping as well as by anomalously light regenerated silicic acid due to iron limitation.

19449224, 2026, 5, Downloaded from https://agupubs.onlinelibrary.wiley.com/doi/10.1029/2025GB009008 by Finnish Meteorological, Wiley Online Library on [29/09/2026]. See the Terms and Conditions (https://onlinelibrary.wiley.com/terms-and-conditions) on Wiley Online Library for rules of use; OA articles are governed by the applicable Creative Commons License

4.3. Variations in Deep Water $\delta^{30}Si_{obs}$

Outside the SO, the deep waters along $GP17_{OCE}$ show strong vertical gradients in $\delta^{30}Si_{obs}$ and nearly constant $\delta^{30}Si_{obs}$ along isopycnals (Figure 2c). Although there is some deviation in the deep waters related to non-linear mixing with the surface of the SO (Section 3.1.3), the average $\delta^{30}Si_{obs}$ and $[Si(OH)_4]^{-1}$ within UCDW, LCDW, and AABW form a tight linear relationship with $R^2 = 0.999$ (Figure 3, inset). This relationship fits the expected mixing, with $[Si(OH)_4]_{obs}$ and decreasing $\delta^{30}Si_{obs}$ associated with increasing density (Figure 3, inset). The model captures these trends well with $\delta^{30}Si$ of both the preformed and regenerated silicic acid (Figures 6m and 7m) becoming progressively lighter with depth and increasing $[Si(OH)_4]_{reg}$ (Figure 5b). In deep waters with $\gamma_n > 27.7$ kg m^{-3}, the polar SO has a slightly lighter average isotopic composition ($1.26 \pm 0.07‰$, $n = 69$) than the South Pacific ($1.32 \pm 0.05‰$, $n = 119$). This difference results from the trapping of light $\delta^{30}Si_{reg}$ in the deep polar SO (Figure 7l) and increasing importance of heavy $\delta^{30}Si_{reg}$ from distal sources north of the SAZ at the northern end of the transect (Figure 7c). Opal dissolution from the oligotrophic gyre is thought to play a minimal role in altering $\delta^{30}Si$ signatures of the deep South Pacific basin (de Souza, Reynolds, Rickli, et al., 2012), consistent with our model showing that heavy $\delta^{30}Si_{reg}$ from distal sources north of the SAZ originate in the eastern tropical Pacific and subpolar North Pacific where high nutrient consumption rates lead to export of heavier $\delta^{30}Si_{reg}$ (Figure 8b).

Growing understanding of $\delta^{30}Si$ in global deep waters has begun to challenge the previous assumption of isotopically homogenous deep-water distributions (Beucher et al., 2008; Brzezinski et al., 2025; Grasse et al., 2020; Reynolds et al., 2006). Similarly, while a number of models predicted an asymptotic value of ~+1.2‰ when $[Si(OH)_4] > 120$ μmol kg^{-1} (de Souza et al., 2014; Gao et al., 2016; Wischmeyer et al., 2003), our measurements of $\delta^{30}Si_{obs}$ in deep waters within the polar SO and South Pacific basin vary substantially. In the polar SO, south of the PF, deep-water samples with $[Si(OH)_4]_{obs} > 120$ μmol kg^{-1} had $\delta^{30}Si_{obs}$ values between 1.19‰ and 1.35‰. North of the PF in the South Pacific, $\delta^{30}Si_{obs}$ fell between 1.23 and 1.40 for similarly $[Si(OH)_4]_{obs}$-rich deep waters, with the lightest $\delta^{30}Si_{obs}$ in the South Pacific occurring relatively far from the polar SO at 37.5°S, just south of the STF. The observed range of $\delta^{30}Si_{obs}$ in deep waters across the transect indicates that the $Si(OH)_4$-rich waters of the deep Pacific and adjacent polar SO are not isotopically homogenous but instead show a high degree of variability.

The control by regenerated silicic acid shown here for $GP17_{OCE}$ contrasts findings in the Atlantic, where de Souza, Reynolds, Rickli, et al. (2012) found that deep-water $\delta^{30}Si_{obs}$ was controlled by the admixture of $[Si(OH)_4]$-rich, isotopically light AABW flowing in through the Drake Passage with $[Si(OH)_4]$-poor, isotopically heavy NADW from the Labrador Sea. The Atlantic has low surface productivity compared to the Pacific, leading to minimal contribution of regenerated silicic acid to Atlantic deep waters during transit (Anderson & Sarmiento, 1994; Broecker et al., 1991; Sarmiento et al., 2007). Silicon-cycling models suggest that the progressive lightening of $\delta^{30}Si$ in deep waters as $[Si(OH)_4]$ increases along the deep path of the MOC is driven by a switch in the relative importance of preformed to regenerated $Si(OH)_4$. Thus, the Atlantic Ocean is dominated by $[Si(OH)_4]_{pre}$ (de Souza et al., 2014), while the accumulation of relatively light $[Si(OH)_4]_{reg}$ along the MOC leads to regenerated silicic acid controlling much of the deep-water Si isotope signatures in the Southern and Pacific Oceans (7 m; de Souza et al., 2014; Gao et al., 2016; Holzer & Brzezinski, 2015; Wischmeyer et al., 2003). Along the deep-water MOC, the modeled global minimum $\delta^{30}Si$ of the deep SO interrupts the lightening trend due to nutrient trapping.

5. Conclusions

We report measurements along a synoptic full-depth section of $\delta^{30}Si_{obs}$ in $Si(OH)_4$ extending from the tropics near Tahiti (20°S) to 60°S in the SO along the meridional portion of $GP17_{OCE}$. The section sampled mode, intermediate, and deep waters and allowed us to assess the controls on the large-scale $\delta^{30}Si$ structure seen in global models. In models, the partitioning of light and heavy silicon isotopes between the upper ocean and deep waters predominantly results from nutrient trapping in the high southern latitudes. Our data are consistent with nutrient trapping and partial nutrient consumption in surface waters leading to the accumulation of light silicon isotopes in the SO, which feeds deep waters globally, while the heavy fraction rejected during opal formation is subducted in mode and intermediate waters and transported northward.

Measurements across the outcropping regions of the mode and intermediate waters captured the subduction of the isotopically heavy silicic acid into both water masses, in agreement with previous conceptualizations of isotope

19449224, 2026, 5, Downloaded from https://agupubs.onlinelibrary.wiley.com/doi/10.1029/2025GB009008 by Finnish Meteorological, Wiley Online Library on [29/09/2026]. See the Terms and Conditions (https://onlinelibrary.wiley.com/terms-and-conditions) on Wiley Online Library for rules of use; OA articles are governed by the applicable Creative Commons License

controls in which subducted heavy $\delta^{30}Si$ is transported from high to low latitudes within mode and intermediate waters (de Souza, Reynolds, Johnson, et al., 2012; Fripiat et al., 2011) and with model results that indicate sources of heavy $\delta^{30}Si_{pre}$ from the outcrops of mode and intermediate waters (de Souza et al., 2014; Holzer & Brzezinski, 2015). The isotopic composition of mode waters in model simulations is modified by the addition of relatively heavy $\delta^{30}Si_{reg}$ sourced from the global ocean north of the SAZ, and heavy $\delta^{30}Si_{pre}$ entrained from UCDW. These sources supplement one another, leading $\delta^{30}Si_{obs}$ within mode and intermediate waters that vary little along isopycnals, consistent with the observations reported here. Entrainment of UCDW contributes 27% and 40% of total modeled $Si(OH)_4$ to SAMW and AAIW, respectively, with much of these contributions coming from distal regenerated sources (Figures 8b and 9b). Beyond their effects on $\delta^{30}Si$, distal sources introduce bias into estimates of respiration and carbon sequestration in SAMW and AAIW (Carter et al., 2014).

In deep waters, models indicate progressive lightening of $\delta^{30}Si$ with increasing $[Si(OH)_4]$ along the global conveyor pathways, driven by the increasing relative importance of isotopically light regenerated $Si(OH)_4$. This general trend is interrupted by the SO $\delta^{30}Si$ minimum due to nutrient trapping. Our observational data agree with this schema, with a minimum of $\delta^{30}Si_{obs} = +1.19‰$ in AABW relative to a minimum of $\delta^{30}Si_{obs} = +1.23‰$ in the deep south Pacific. Our model indicates that the $\delta^{30}Si_{reg}$ contribution to the SO $\delta^{30}Si$ minimum is sourced from the polar SO itself, in agreement with SO silicic-acid trapping and near chronic partial nutrient consumption in polar surface waters producing exceptionally light $\delta^{30}Si_{reg}$. Deep waters of the South Pacific basin exhibited strong vertical gradients in $\delta^{30}Si_{obs}$ and nearly constant $\delta^{30}Si_{obs}$ along isopycnals, with the increasing fractional contribution of $[Si(OH)]_{reg}$ leading to progressively lighter $\delta^{30}Si_{obs}$ with depth.

Conflict of Interest

The authors declare no conflicts of interest relevant to this study.

Availability Statement

All NSF funded data used in this report are archived at the Biological and Chemical Oceanography Data Management Office at BCO-DMO https://www.bco-dmo.org/dataset/991532 (Brzezinski et al., 2026; https://doi.org/10.26008/1912/bco-dmo.991532.1) and https://www.bco-dmo.org/dataset/933861 (Twining et al., 2025; https://doi.org/10.26008/1912/bco-dmo.933861.2).

Acknowledgments
We would like to thank the officers, crew and scientific party members aboard R/V Roger Revelle during the 2022 GEOTRACES GP17-OCE cruise for their help during all aspects of our operations. We particularly thank Martin Fleisher, who collected the isotope samples at sea. Our thanks also go to the chemistry group of the Oceanography Data Facility at Scripps Oceanographic Institution for silicic acid, phosphate, and oxygen analyses. Support was provided through the National Science Foundation Chemical Oceanography program to MAB (OCE-2048998). The International GEOTRACES Program is possible in part thanks to the support from the U.S. National Science Foundation (OCE-2140395) to the Scientific Committee on Oceanic Research (SCOR).

References

Anderson, L. A., & Sarmiento, J. L. (1994). Redfield ratios of remineralization determined by nutrient data analysis. *Global Biogeochemical Cycles*, *8*(1), 65–80. https://doi.org/10.1029/93GB03318

Becker, S., Aoyama, M., Woodward, E. M. S., Bakker, K., Coverly, S., Mahaffey, C., & Tanhua, T. (2019). The precise and accurate determination of dissolved inorganic nutrients in seawater; continuous flow analysis methods and laboratory practices. *GO-SHIP Repeat Hydrography Manual: A Collection of Expert Reports and Guidelines*, *14*.

Beucher, C. P., Brzezinski, M. A., & Jones, J. L. (2008). Sources and biological fractionation of silicon isotopes in the eastern equatorial Pacific. *Geochimica et Cosmochimica Acta*, *72*(13), 3063–3073. https://doi.org/10.1016/j.gca.2008.04.021

Bostock, H. C., Sutton, P. J., Williams, M. J. M., & Opdyke, B. N. (2013). Reviewing the circulation and mixing of Antarctic intermediate water in the South Pacific using evidence from geochemical tracers and Argo float trajectories. *Deep-Sea Research Part I Oceanographic Research Papers*, *73*, 84–98. https://doi.org/10.1016/j.dsr.2012.11.007

Broecker, W. S., Blanton, S., Smethie, W. M., Lamont-Doherty, J., & Ostlund, G. (1991). Radiocarbon decay and oxygen utilization in the deep Atlantic Ocean. *Global Biogeochemical Cycles*, *5*(1), 7–117. https://doi.org/10.1029/90gb02279

Brzezinski, M. A. (2024). Depth profiles of the isotopic composition (δ30Si) of silicon within dissolved silicic acid from samples collected on Leg 2 of the US GEOTRACES pacific meridional transect (PMT) cruise (GP15, RR1815) on R/V roger revelle from October to November 2018 (version 1) [Dataset]. *Biological and Chemical Oceanography Data Management Office (BCO-DMO)*. https://doi.org/10.26008/1912/BCO-DMO.946249.1

Brzezinski, M. A., Closset, I., Holzer, M., & Jones, J. L. (2025). The silicon isotopic composition of the North Pacific: Insights from US GEOTRACES section GP15 and modeling. *Global Biogeochemical Cycles*, *39*(12), e2025GB008557. https://doi.org/10.1029/2025GB008557

Brzezinski, M. A., Closset, I., & Middleton, J. (2026). Silicon stable isotopes for samples collected from surface to depth on the US GEOTRACES GP17-OCE cruise on R/V Roger Revelle (RR2214) from December 2022 to January 2023 (version 1) [Dataset]. *Biological and Chemical Oceanography Data Management Office (BCO-DMO)*. https://doi.org/10.26008/1912/BCO-DMO.991532.1

Brzezinski, M. A., Dickson, M.-L., Nelson, D. M., & Sambrotto, R. (2003). Ratios of Si, C and N uptake by microplankton in the Southern Ocean. *Deep Sea Research Part II: Topical Studies in Oceanography*, *50*(3–4), 619–633. https://doi.org/10.1016/S0967-0645(02)00587-8

Brzezinski, M. A., & Jones, J. L. (2015). Coupling of the distribution of silicon isotopes to the meridional overturning circulation of the North Atlantic Ocean. *Deep-Sea Research Part II Topical Studies in Oceanography*, *116*, 79–88. https://doi.org/10.1016/j.dsr2.2014.11.015

Brzezinski, M. A., Jones, J. L., Beucher, C. P., Demarest, M. S., & Berg, H. L. (2006). Automated determination of silicon isotope natural abundance by the acid decomposition of cesium hexafluosilicate. *Analytical Chemistry*, *78*(17), 6109–6114. https://doi.org/10.1021/ac0606406

Cardinal, D., Alleman, L. Y., Dehairs, F., Savoye, N., Trull, T. W., & André, L. (2005). Relevance of silicon isotopes to Si-nutrient utilization and Si-source assessment in Antarctic waters. *Global Biogeochemical Cycles*, *19*(2), 1–13. https://doi.org/10.1029/2004GB002364

Cardinal, D., Savoye, N., Trull, T. W., Dehairs, F., Kopczynska, E. E., Fripiat, F., et al. (2007). Silicon isotopes in spring Southern Ocean diatoms: Large zonal changes despite homogeneity among size fractions. *Marine Chemistry*, *106*(1–2), 46–62. https://doi.org/10.1016/j.marchem.2006.04.006

Carter, B. R., Talley, L. D., & Dickson, A. G. (2014). Mixing and remineralization in waters detrained from the surface into subantarctic mode water and Antarctic intermediate water in the southeastern Pacific. *Journal of Geophysical Research: Oceans*, *119*(6), 4001–4028. https://doi.org/10.1002/2013JC009355

Cavagna, A. J., Fripiat, F., Dehairs, F., Wolf-Gladrow, D., Cisewski, B., Savoye, N., et al. (2011). Silicon uptake and supply during a Southern Ocean iron fertilization experiment (EIFEX) tracked by Si isotopes. *Limnology and Oceanography*, *56*(1), 147–160. https://doi.org/10.4319/lo.2011.56.1.0147

Closset, I., Cardinal, D., Bray, S. G., Thil, F., Djouraev, I., Rigual-Hernández, A. S., & Trull, T. W. (2015). Seasonal variations, origin, and fate of settling diatoms in the Southern Ocean tracked by silicon isotope records in deep sediment traps. *Global Biogeochemical Cycles*, *29*(9), 1495–1510. https://doi.org/10.1002/2015GB005180

Closset, I., Cardinal, D., Rembauville, M., Thil, F., & Blain, S. (2016). Unveiling the Si cycle using isotopes in an iron-fertilized zone of the Southern Ocean: From mixed-layer supply to export. *Biogeosciences*, *13*(21), 6049–6066. https://doi.org/10.5194/bg-13-6049-2016

Cutter, G., Casciotti, K., Croot, P., Geibert, W., Heimbürger, L.-E., Lohan, M., et al. (2017). Sampling and sample-handling protocols for GEOTRACES cruises. Version 3, August 2017. GEOTRACES International Project Office.

De La Rocha, C., Brzezinski, M. A., & Deniro, M. J. (2000). A first look at the distribution of the stable isotopes of silicon in natural waters. *Geochimica et Cosmochimica Acta*, *64*(12), 2467–2477. https://doi.org/10.1016/s0016-7037(00)00373-2

De La Rocha, C. L., Brzezinski, M. A., & DeNiro, M. J. (1996). Purification, recovery, and Laser-DrivenFluorination of silicon from dissolved and particulate Silica for the measurement of natural stable isotope abundances. *Geochimica et Cosmochimica Acta*, *66*(2), 17.

De Lavergne, C., Vic, C., Madec, G., Roquet, F., Waterhouse, A. F., Whalen, C. B., et al. (2020). A parameterization of local and remote tidal mixing. *Journal of Advances in Modeling Earth Systems*, *12*(5), e2020MS002065. https://doi.org/10.1029/2020MS002065

de Souza, G. F., Reynolds, B. C., Johnson, G. C., Bullister, J. L., & Bourdon, B. (2012). Silicon stable isotope distribution traces Southern Ocean export of Si to the eastern South Pacific thermocline. *Biogeosciences*, *9*(11), 4199–4213. https://doi.org/10.5194/bg-9-4199-2012

de Souza, G. F., Reynolds, B. C., Rickli, J., Frank, M., Saito, M. A., Gerringa, L. J. A., & Bourdon, B. (2012). Southern Ocean control of silicon stable isotope distribution in the deep Atlantic Ocean. *Global Biogeochemical Cycles*, *26*(2). https://doi.org/10.1029/2011GB004141

de Souza, G. F., Slater, R. D., Dunne, J. P., & Sarmiento, J. L. (2014). Deconvolving the controls on the deep ocean's silicon stable isotope distribution. *Earth and Planetary Science Letters*, *398*, 66–76. https://doi.org/10.1016/j.epsl.2014.04.040

DeVries, T., & Primeau, F. (2011). Dynamically and observationally constrained estimates of water-mass distributions and ages in the global ocean. *Journal of Physical Oceanography*, *41*(12), 2381–2401. https://doi.org/10.1175/JPO-D-10-05011.1

Franck, V. M., Brzezinski, M. A., Coale, K. H., & Nelson, D. M. (2000). Iron and silicic acid concentrations regulate Si uptake north and south of the polar frontal zone in the Pacificc sector of the Southern Ocean. *Deep Sea Research II*, *47*, 3315–3338. https://doi.org/10.1016/S0967-0645(00)00070-9

Fripiat, F., Cavagna, A. J., Dehairs, F., De Brauwere, A., André, L., & Cardinal, D. (2012). Processes controlling the Si-isotopic composition in the Southern Ocean and application for paleoceanography. *Biogeosciences*, *9*(7), 2443–2457. https://doi.org/10.5194/bg-9-2443-2012

Fripiat, F., Cavagna, A. J., Dehairs, F., Speich, S., André, L., & Cardinal, D. (2011). Silicon pool dynamics and biogenic silica export in the Southern Ocean inferred from Si-isotopes. *Ocean Science*, *7*(5), 533–547. https://doi.org/10.5194/os-7-533-2011

Gao, S., Wolf-Gladrow, D. A., & Völker, C. (2016). Simulating the modern δ30Si distribution in the oceans and in marine sediments. *Global Biogeochemical Cycles*, *30*(2), 120–133. https://doi.org/10.1002/2015GB005189

Garcia, H., Weathers, K., Paver, C., Smolyar, I., Boyer, T., Locarnini, R., et al. (2018). Dissolved inorganic nutrients (phosphate, nitrate and nitrate+nitrite, silicate). In A. Mishonov (Ed.), *World ocean atlas* (Vol. 4). NOAA Atlas NESDIS

Gnanadesikan, A. (1999). A global model of silicon cycling: Sensitivity to eddy parameterization and dissolution. *Global Biogeochemical Cycles*, *13*(1), 199–220. https://doi.org/10.1029/1998GB900013

Grasse, P., Brzezinski, M. A., Cardinal, D., De Souza, G. F., Andersson, P., Closset, I., et al. (2017). GEOTRACES inter-calibration of the stable silicon isotope composition of dissolved silicic acid in seawater. *Journal of Analytical Atomic Spectrometry*, *32*(3), 562–578. https://doi.org/10.1039/C6JA00302H

Grasse, P., Closset, I., Jones, J. L., Geilert, S., & Brzezinski, M. A. (2020). Controls on dissolved silicon isotopes along the U.S. GEOTRACES Eastern Pacific zonal transect (GP16). *Global Biogeochemical Cycles*, *34*(9), e2020GB006538. https://doi.org/10.1029/2020GB006538

Gutiérrez-Rodríguez, A., Latasa, M., Safi, K., Pinkerton, M. H., & Nodder, S. D. (2023). Decoupled growth and grazing rates of diatoms and green algae drive increased phytoplankton productivity on HNLC sub- Antarctic plateaux. *Limnology and Oceanography Letters*, *8*(6), 896–905. https://doi.org/10.1002/lol2.10355

Hartin, C. A., Fine, R. A., Sloyan, B. M., Talley, L. D., Chereskin, T. K., & Happell, J. (2011). Formation rates of Subantarctic mode water and Antarctic intermediate water within the South Pacific. *Deep-Sea Research Part I Oceanographic Research Papers*, *58*(5), 524–534. https://doi.org/10.1016/j.dsr.2011.02.010

Holzer, M., & Brzezinski, M. A. (2015). Controls on the silicon isotope distribution in the ocean: New diagnostics from a data-constrained model. *Global Biogeochemical Cycles*, *29*(3), 267–287. https://doi.org/10.1002/2014GB004967

Holzer, M., DeVries, T., & De Lavergne, C. (2021). Diffusion controls the ventilation of a Pacific Shadow zone above abyssal overturning. *Nature Communications*, *12*(1), 4348. https://doi.org/10.1038/s41467-021-24648-x

Holzer, M., Primeau, F. W., DeVries, T., & Matear, R. (2014). The Southern Ocean silicon trap: Data-constrained estimates of regenerated silicic acid, trapping efficiencies, and global transport paths. *Journal of Geophysical Research: Oceans*, *119*(1), 313–331. https://doi.org/10.1002/2013JC009356

Jutras, M., Bushinsky, S. M., Cerovečki, I., & Briggs, N. (2025). Mixing accounts for more than half of biogeochemical changes along mode water ventilation pathways. *Geophysical Research Letters*, *52*(7), e2024GL113789. https://doi.org/10.1029/2024GL113789

Kay, A. (2001). Thermobaric flow. *Dynamics of Atmospheres and Oceans*, *34*(2–4), 263–289. https://doi.org/10.1016/s0377-0265(01)00071-9

Langdon, C. (2010). Determination of dissolved oxygen in seawater by winkler titration using the amperometric technique. *GO-SHIP Repeat Hydrography Manual*, *14*.

Li, Z., England, M. H., Groeskamp, S., Cerovečki, I., & Luo, Y. (2021). The origin and fate of subantarctic mode water in the Southern Ocean. *Journal of Physical Oceanography*. https://doi.org/10.1175/JPO-D-20-0174.1

Li, Z., Groeskamp, S., Cerovečki, I., & England, M. H. (2022). The origin and fate of antarctic intermediate water in the Southern Ocean. *Journal of Physical Oceanography*, *52*(11), 2873–2890. https://doi.org/10.1175/jpo-d-21-0221.1

Lumpkin, R., & Speer, K. (2007). Global ocean meridional overturning. *Journal of Physical Oceanography*, *37*(10), 2550–2562. https://doi.org/10.1175/JPO3130.1

19449224, 2026, 5, Downloaded from https://agupubs.onlinelibrary.wiley.com/doi/10.1029/2025GB009008 by Finnish Meteorological, Wiley Online Library on [29/09/2026]. See the Terms and Conditions (https://onlinelibrary.wiley.com/terms-and-conditions) on Wiley Online Library for rules of use; OA articles are governed by the applicable Creative Commons License

McDougall, T. J. (1987). Thermobaricity, cabbeling, and water-mass conversion. *Journal of Geophysical Research*, *92*(C5), 5448–5464. https://doi.org/10.1029/JC092iC05p05448

Orsi, A. H., Whitworth III, T., & Nowlin, W. D. (1995). On the meridional extent and fronts of the Antarctic circumpolar current. *Deep-Sea Research I*, *42*(5), 64–673. https://doi.org/10.1016/0967-0637(95)00021-w

Palter, J. B., Sarmiento, J. L., Gnanadesikan, A., Simeon, J., & Slater, D. (2010). Nutrient return pathways fueling primary productivity: Nutrient return pathways from the deep ocean and their dependence on the meridional overturning circulation nutrient return pathways. *Biogeosciences Discussions*, *7*, 4045–4088. https://doi.org/10.5194/bgd-7-4045-2010

Paul, D., Skrzypek, G., & Fórizs, I. (2007). Normalization of measured stable isotopic compositions to isotope reference scales – A review. *Rapid Communications in Mass Spectrometry*, *21*(18), 3006–3014. https://doi.org/10.1002/rcm.3185

Primeau, F. W., Holzer, M., & DeVries, T. (2013). Southern Ocean nutrient trapping and the efficiency of the biological pump. *Journal of Geophysical Research: Oceans*, *118*(5), 2547–2564. https://doi.org/10.1002/jgrc.20181

Reynolds, B. C., Aggarwal, J., André, L., Baxter, D., Beucher, C., Brzezinski, M. A., et al. (2007). An inter-laboratory comparison of Si isotope reference materials. *Journal of Analytical Atomic Spectrometry*, *22*(5), 561–568. https://doi.org/10.1039/b616755a

Reynolds, B. C., Georg, R. B., Oberli, F., Wiechert, U., & Halliday, A. N. (2006). Re-assessment of silicon isotope reference materials using high-resolution multi-collector ICP-MS. *Journal of Analytical Atomic Spectrometry*, *21*(3), 266–269. https://doi.org/10.1039/b515908c

Sarmiento, J. L., & Gruber, N. (2006). *Ocean biogeochemical dynamics*. Princeton University Press.

Sarmiento, J. L., Gruber, N., Brzezinski, M. A., & Dunne, J. P. (2004). High-latitude controls of thermocline nutrients and low latitude biological productivity. *Nature*, *427*(6969), 56–60. https://doi.org/10.1038/nature10605

Sarmiento, J. L., Simeon, J., Gnanadesikan, A., Gruber, N., Key, R. M., & Schlitzer, R. (2007). Deep ocean biogeochemistry of silicic acid and nitrate. *Global Biogeochemical Cycles*, *21*(1). https://doi.org/10.1029/2006GB002720

Sutton, J. N., André, L., Cardinal, D., Conley, D. J., De Souza, G. F., Dean, J., et al. (2018). A review of the stable isotope bio-geochemistry of the global silicon cycle and its associated trace elements. *Frontiers in Earth Science*, *5*, 112. https://doi.org/10.3389/feart.2017.00112

Sutton, J. N., Varela, D. E., Brzezinski, M. A., & Beucher, C. P. (2013). Species-dependent silicon isotope fractionation by marine diatoms. *Geochimica et Cosmochimica Acta*, *104*, 300–309. https://doi.org/10.1016/j.gca.2012.10.057

Talley, L. D. (2013). Closure of the global overturning circulation through the Indian, Pacific, and southern oceans. *Oceanography*, *26*(1), 80–97. https://doi.org/10.5670/oceanog.2013.07

Talley, L. D., Pickard, G. L., Emery, W. J., & Swift, J. H. (2011). Introduction to descriptive physical oceanography. In *Descriptive physical oceanography* (pp. 1–6). Elsevier. https://doi.org/10.1016/B978-0-7506-4552-2.10001-0

Tréguer, P., Bowler, C., Moriceau, B., Dutkiewicz, S., Gehlen, M., Aumont, O., et al. (2018). Influence of diatom diversity on the ocean biological carbon pump. *Nature Geoscience*, *11*(1), 27–37. https://doi.org/10.1038/s41561-017-0028-x

Twining, B., Cutter, G. A., & Fitzsimmons, J. N. (2025). Nutrients and bottle oxygen measured by the Scripps ODF group on the US GEOTRACES GP17-OCE cruise on R/V Roger Revelle (RR2214) from December 2022 to January 2023 in the South Pacific and Southern Oceans (version 2) [Dataset]. *Biological and Chemical Oceanography Data Management Office (BCO-DMO)*. https://doi.org/10.26008/1912/BCO-DMO.933861.2

Varela, D. E., Pride, C. J., & Brzezinski, M. A. (2004). Biological fractionation of silicon isotopes in Southern Ocean surface waters. *Global Biogeochemical Cycles*, *18*(1). https://doi.org/10.1029/2003gb002140

Williams, N. L., Juranek, L. W., Johnson, K. S., Feely, R. A., Riser, S. C., Talley, L. D., et al. (2016). Empirical algorithms to estimate water column pH in the Southern Ocean. *Geophysical Research Letters*, *43*(7), 3415–3422. https://doi.org/10.1002/2016GL068539

Wischmeyer, A. G., De La Rocha, C. L., Maier-Reimer, E., & Wolf-Gladrow, D. A. (2003). Control mechanisms for the oceanic distribution of silicon isotopes. *Global Biogeochemical Cycles*, *17*(3). https://doi.org/10.1029/2002gb002022

Erratum

The originally published version of this article contained an error. The fifth sentence of the first paragraph of Section 2.5 has been corrected as follows: "We prescribed a biological uptake timescale of 10.5 days and optimized the opal sinking speed (38.7 m d^{-1}) and burial fraction (10.6%) by minimizing the volume-weighted globally integrated quadratic mismatch between modeled [$Si(OH)_4$] and the WOA18 observations." This may be considered the authoritative version of record.

19449224, 2026, 5, Downloaded from https://agupubs.onlinelibrary.wiley.com/doi/10.1029/2025GB009008 by Finnish Meteorological, Wiley Online Library on [29/09/2026]. See the Terms and Conditions (https://onlinelibrary.wiley.com/terms-and-conditions) on Wiley Online Library for rules of use; OA articles are governed by the applicable Creative Commons License